

Computational modelling of dynamic recrystallisation of Ni-based superalloy during linear friction welding

Saviour I. Okeke^{1,2,3}, Noel M. Harrison^{1,2,3*}, Mingming Tong^{1,2,3}

¹Mechanical Engineering, School of Engineering, College of Science and Engineering, NUI Galway, Galway, Ireland.

²I-Form, the SFI Research Centre for Advanced Manufacturing, Dublin, Ireland.

³Ryan Institute for Environmental, Marine and Energy Research, NUI Galway, Galway, Ireland.

*Corresponding author email: noel.harrison@nuigalway.ie

Abstract

Linear friction welding (LFW) is an advanced joining technology used for manufacturing and repairing complex assemblies like blade integrated disks (blisks) of aeroengines. This paper presents an integrated multiphysics computational modelling for predicting the thermomechanical-microstructural processes of IN718 alloy (at the component-scale) during LFW. Johnson-Mehl-Avrami-Kolmogorov (JMAK) model was implemented for predicting the dynamic recrystallisation of γ grain, which was coupled with thermomechanical modelling of the LFW process. The computational modelling results of this paper agree well with experimental results from the literature in terms of γ grain size and weld temperature. Twenty different LFW process parameter configurations were systematically analysed in the computations by using the integrated model. It was found that friction pressure was the most influential process parameter, which significantly affected the dynamic recrystallisation of γ grains and weld temperature during LFW. The integrated multiphysics computational modelling was employed to find the appropriate process window of IN718 LFW.

Keywords

Linear friction welding, Inconel 718, dynamic recrystallisation, gamma grain, microstructural modelling, multiphysics modelling

Nomenclature

Acronyms and Greek	
DRX	Dynamic Recrystallisation
IN718	Inconel 718
JMAK	Johnson-Mehl-Avrami-Kolmogorov
LFW	Linear friction welding

Ni	Nickel
α_w	Thermal expansion [K^{-1}]
δ	Delta phase
ε	Plastic strain
$\dot{\varepsilon}$	Strain rate [s^{-1}]
ε_c	Critical strain
ε_p	Peak strain
$\varepsilon_{0.5}$	Plastic strain for 50% recrystallised volume fraction
$\varepsilon_{c1}, \varepsilon_{b1}$	IN718 DRX constants
η	Efficiency of converting mechanical energy to heat energy
γ	Gamma grain
γ'	Gamma prime phase
γ''	Gamma double prime phase
λ	Thermal conductivity [$W \cdot m^{-1} K^{-1}$]
μ	Coulomb's friction coefficient
ν	Poisson's ratio
ϕ	Emissivity
ρ	Density [$kg \cdot m^{-3}$]
σ_e	Effective stress [MPa]
σ_s	Shear stress [MPa]
σ_y	Yield stress [MPa]
τ_{fr}	Frictional shear stress [MPa]
θ	Stefan–Boltzmann constant [$W \cdot m^{-2} K^{-4}$]
VUHARD	Abaqus/Explicit user-hardening subroutine

Abbreviations	Unit	Term
A_0	mm	Oscillating amplitude
$A(\varepsilon), n(\varepsilon), \alpha(\varepsilon)$		IN718 material constants
c_p	$J \cdot kg^{-1} K^{-1}$	Specific heat capacity
d_0	μm	Initial γ grain size
D_{ave}	μm	Average γ grain size
d_{DRX}	μm	Recrystallised γ grain size
F	$N \cdot kg^{-1}$	Body force vector per unit mass
f_0	Hz	Oscillating frequency
$g_{c1}, g_{c2}, g_{c3}, g_{l1}, g_{l2}, g_{l3}, n_{b1}, n_{c1}$		IN718 DRX constants
h_k	$W \cdot m^{-2} K^{-1}$	Convective heat transfer coefficient
L_a	mm	Axial shortening
n	m^2	Surface area of workpiece
n_d		Avrami constant
p_f	MPa	Friction pressure
$Q(\varepsilon)$	$J \cdot mol^{-1}$	Deformation activation energy

R	$\text{J}\cdot\text{mol}^{-1}\text{K}^{-1}$	Gas constant
t	s	Time
t_k	s	Current step time
t_{k-1}	s	Previous step time
T	K	Weld temperature
T_c	K	Ambient temperature
T_w	K	Wall (boundary) temperature
v_s	$\text{mm}\cdot\text{s}^{-1}$	Slip velocity
v_r	$\text{mm}\cdot\text{s}^{-1}$	Average rubbing velocity
X_{DRX}		Recrystallised volume fraction
Z	s^{-1}	Zener-Hollomon parameter

1 Introduction

2 Linear friction welding (LFW) is an advanced energy-efficient solid-state joining technology,
3 which has important application in the manufacture of critical engineering components such as in
4 the aerospace industry. LFW can produce high-quality welds by rapidly oscillating one workpiece
5 relative to another while applying large compressive pressure. During LFW, friction heat is
6 generated between the oscillating and stationary workpieces, leading to material softening and
7 bonding of workpieces under sustained pressure. Unlike conventional fusion welding, the
8 contacting surfaces of workpieces are welded together without remelting of the surfaces during
9 LFW. LFW can join similar and dissimilar materials and a wide range of materials have been
10 successfully joined, such as titanium alloys, aluminium alloys, and steels, with the foremost
11 industrial application in aeroengine alloys of blade integrated disks (blisks) [1-8]. Despite the
12 increasing application of LFW, the complex interaction between heat transfer, deformation of weld
13 and material microstructural evolution during LFW is not well understood.

14 Inconel 718 (IN718) is one of the Ni-based superalloys, which has excellent high-temperature
15 strength, strong oxidation resistance, and high corrosion resistance. It has been widely applied in
16 modern aero-engines, steam turbine power plants, nuclear power systems, and marine and oil
17 applications [8-11]. In precipitation strengthened IN718, the primary (γ) phase and secondary (γ' ,
18 γ'' and δ) have a direct influence on mechanical properties of the alloy. γ'' (Ni_3Nb) and γ' (Ni_3Al)
19 are the primary and secondary strengthening precipitates, respectively. The δ phase has the same
20 composition as the γ'' phase, precipitates at the grain boundaries, and can prevent grain boundary
21 migration [12-14]. These primary and secondary phases of IN718 undergo significant
22 microstructural change during thermomechanical processing, due to elevated temperature and
23 significant material deformation, which can significantly affect the mechanical properties of
24 manufactured components.

25 Several studies have reported the influence of thermomechanical processes on the microstructural
26 properties and resultant mechanical behaviour of IN718 during LFW [11,15-18]. For instance, it
27 was found that the level of friction heat generated at the friction interface of the weld could directly
28 determine the local hardness profile (as well as the γ grain size and γ' volume fraction) of an IN718
29 LFW weld joint [11,18]. Markov et al. used the Maxwell visco-elastic model for predicting the
30 thermomechanical processes of steel, which is not popularly used for computational modelling of
31 IN718 LFW like the strain-compensated Arrhenius equation in Qin et al. [19,20]. The dynamic
32 recrystallisation of γ grains during LFW might refine material microstructure and increase the
33 hardness and tensile strength of weld [20-23]. In some studies, the hardness profile at the friction
34 interface was attributed to a combination of variation in γ grain size, γ' volume fraction, size and
35 distribution, γ - γ' misfit, and work hardening due to residual plastic work [23-26]. Mary and Jahazi
36 noted that dynamic recrystallisation and dynamic recovery of γ grains occur simultaneously with
37 the loss of the δ phase in IN718 weld joint during LFW [16]. They reported that γ grains within
38 ± 1 mm distance from the friction interface were three times smaller than those of the parent
39 material (16 μm) because DRX occurred during LFW [16]. In another study, Mary and Jahazi
40 observed that beyond 3-mm distance from the friction interface, the γ grain size remains constant
41 and equal to the γ grain size of the base metal (non-welded) material and the temperature is below

42 the δ phase equilibrium solvus temperature (~ 1283 K) [17]. Similarly, Chamanfar et al. observed
43 fine γ grain size of $7.5 \mu\text{m}$ within 0.9 mm of the friction interface of linear friction welded
44 Waspaloy, whereas the parent material grain size was $15.1 \mu\text{m}$ [25]. Similar grain refinement at
45 the friction interface zone was reported for inertia friction welding of RR@1000 Ni-based
46 superalloy [27,28]. Li et al. found that the presence of γ' phase can hinder DRX; hence, the
47 occurrence of DRX is usually observed in the region where intergranular and intragranular γ' are
48 dissolved [29]. Overall, the recrystallised γ grain size has been consistently recognised as an
49 important factor in refining material microstructure of the weld and directly determining the
50 hardness and tensile strength of weld [30-32]. In order to optimise the design of LFW process
51 parameters, the influence of thermomechanical processes on the microstructural evolution of
52 IN718 needs to be systematically and quantitatively analysed in relation to the DRX of γ grain
53 during LFW process.

54 LFW process optimisation can be achieved by experimentally varying three important welding
55 parameters of such as friction pressure, oscillating frequency, and oscillating amplitude. Multiple
56 researchers have reported the influence of different LFW parameter configurations on such as weld
57 temperature, heating rate, and resultant microstructure and mechanical properties of IN718 weld
58 [20,33-35]. Ma et al. found that DRX and dynamic recovery (DRV) could be enhanced by
59 increasing the friction pressure and oscillating amplitude of LFW [18]. Similar results of enhanced
60 DRX were reported in other research studies [36-38]. Geng et al. noted that the high plastic flow
61 stresses of IN718 at high temperatures were related to the undeformed morphology of numerous
62 refined grains in the thermomechanically affected zone (TMAZ) of IN718 weld [11]. Chamanfar
63 et al., Geng et al., and Masoumi et al. have shown in different studies that grain size is dependent
64 on temperature and strain rate, which are determined by friction pressure, oscillating frequency,
65 and oscillating amplitude [8,11,36]. However, temperature and strain rate, as well as their
66 influence on grain size, are difficult to measure during LFW using experimental methods because
67 LFW is a very dynamic process, which involves very rapid relative motion of workpieces under
68 high pressure [8,11,36]. Several experimental studies on LFW used indirect measurement
69 techniques (e.g. infrared thermal imaging, thermocouple) to estimate weld temperature, strain rate,
70 plastic strain, and stress distribution because direct measurement of LFW process is relatively
71 difficult [8,36]. Xie et al. used a deformation-driven metallurgy method to sinter an aluminium
72 matrix composite reinforced by graphene nanoplatelets, during which the friction heat and plastic
73 deformation caused significant DRX of aluminium grains [39].

74 Computational modelling methods can effectively predict thermomechanical processes as well as
75 material microstructural evolution during materials processing. Such methods have been widely
76 researched and published particularly for the thermomechanical processes of IN718 LFW
77 [20,33,35,40-45]. However, there has been very little work published in relation to the
78 computational modelling for the material microstructural evolution during IN718 LFW.
79 Computational modelling studies about DRX processes have been published for steel, aluminium
80 alloys and titanium alloys during hot forging or hot isothermal compression testing processes
81 [30,46-52]. While these studies have used renowned models such as the Johnson–Mehl–Avrami–
82 Kolmogorov (JMAK) model and the Cellular Automaton model, they have not been implemented
83 for modelling of DRX of γ grains during LFW of IN718 (or any nickel-based superalloy)

84 [30,46,51,53,54]. The authors previously developed an integrated multiphysics computational
85 model for predicting the microstructural evolution of δ phase during LFW of IN718 at the
86 component scale [34]. By using a similar concept of multiphysics computational modelling, a new
87 integrated computational modelling was developed for predicting the DRX of γ grains during LFW
88 of IN718. In Section 2 of this paper, the thermomechanical model for the material response, the
89 microstructural model for the DRX of γ grains, and their coupling for LFW modelling of IN718
90 are presented.

91

92 **2 Modelling method**

93 The integrated multiphysics computational modelling was developed by sequentially coupling a
94 thermomechanical submodel for the LFW process to a microstructural submodel for DRX of γ
95 grains in IN718 alloy. The overall integrated model was implemented in two-dimensional (2D)
96 computational modelling for IN718 LFW by using finite element software package ABAQUS in
97 conjunction with a custom written user-hardening subroutine (VUHARD) [55].

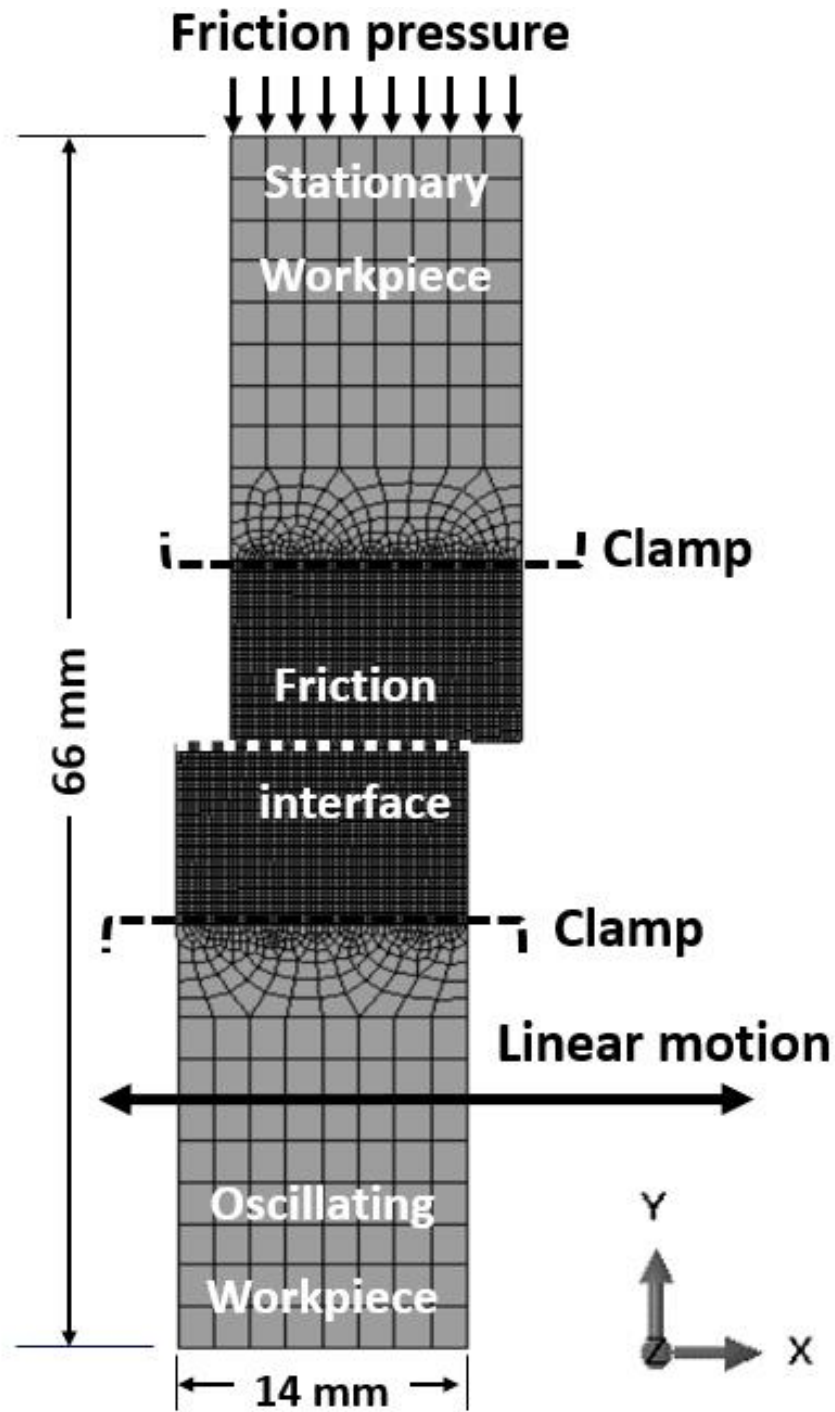
98

99 **2.1 Thermomechanical model**

100 **2.1.1 Set-up of thermomechanical model**

101 The thermomechanical model for LFW of IN718 was implemented by using dynamic temperature-
102 displacement analysis in the Abaqus/Explicit solver, which is suitable for resolving contact
103 problems as well as overcoming excessive element distortion by dynamic remeshing [55]. Similar
104 thermomechanical modelling was previously presented by the authors, in which comprehensive
105 presentations of the thermal and mechanical sub-models of IN718 during LFW can be found in
106 [33,34]. The thermal sub-model and mechanical sub-model are fully coupled. The LFW process
107 lasts for 5.0 s of welding time. The geometry and mesh of the simulation domain are schematically
108 shown in Fig. 1, which consist of a top (oscillating) workpiece and a bottom (stationary)
109 workpiece, contacting each other at the friction interface as a deformable friction pair. The
110 workpieces were discretised using the deformable plane strain formulation with elements defined
111 in the X-Y plane and restricting deformation only to the defined plane. Both workpieces have the
112 same dimension of 33 mm by 14 mm, and the computational domain of each workpiece comprises
113 two structured mesh zones and one unstructured mesh zone. The workpiece dimensions were taken
114 from Geng et al. and Qin et al. and their experimental data (corresponding to LFW setup J13 in
115 this paper) was used by the authors for model verification [11,20].

116



117

118 **Fig. 1** Setup of the 2D simulation domain as well as computational mesh of the friction-paired
 119 deformable workpieces

120

121 In this study, element types of CPE4RT and CPE3T (4-node and 3-node thermally coupled,
 122 displacement and temperature, reduced integration, hourglass control) were specified on the 2D
 123 model. A fine mesh of element size ~0.3 mm was used within 10-mm distance from the friction

124 interface, in the region where high temperature and high plastic deformation happens. Coarse mesh
 125 of size ~1.8 mm was used in the region of the workpieces beyond 10 mm of the friction interface,
 126 where relatively low temperature and low plastic deformation happens. A mesh convergence study
 127 for the thermomechanical model has been presented previously by the authors in [33,34]. There
 128 are 5978 elements and 6170 nodes for the entire simulation domain at the start of computation. To
 129 control excessive distortion of computational mesh domain during material softening and extrusion
 130 of LFW process, the arbitrary Lagrangian-Eulerian (ALE) adaptive dynamic remeshing was
 131 implemented for automatic solution mapping in the Abaqus/Explicit solver [55]. The semi-
 132 automatic mass scaling criterion was specified using a constant value of 800 at the beginning of
 133 each dynamic temperature-displacement explicit analysis step [55,56]. This semi-automatic mass
 134 scaling criterion is commonly used because it limits the kinematic energy to less than 5% of the
 135 internal energy as well as reduces computational cost [6,40,41].

136

137 **2.1.2 Thermal and mechanical behaviour**

138 The thermomechanical model of this study mathematically formulates the thermal and mechanical
 139 responses of IN718 material. The heat diffusion equation is expressed as [20,42,57]:

140

$$\rho C_p \frac{\partial T}{\partial t} = \nabla \cdot \lambda \nabla T + \eta \bar{\sigma} \dot{\epsilon}^{pl} \quad (1)$$

141

142 where ρ is material density in kgm^{-3} , C_p is specific heat capacity in $\text{Jkg}^{-1}\text{K}^{-1}$, λ is temperature-
 143 dependant thermal conductivity in $\text{Wm}^{-1}\text{K}^{-1}$, T is temperature in Kelvin, and t is time in seconds.
 144 η , $\bar{\sigma}$, and $\dot{\epsilon}^{pl}$ are efficiency of converting mechanical energy to heat energy, effective stress in
 145 MPa, and plastic strain rate in s^{-1} , respectively. Mechanical energy efficiency η is specified as 0.9
 146 and the inelastic heat fraction is set to 0.9. During LFW, interfacial frictional heat is conducted
 147 through the contacting surfaces, while convective and radiative heat losses (to the ambient
 148 environment) occur simultaneously. The thermal boundary condition is described as:

$$\lambda \frac{\partial T}{\partial n} = \eta \tau_{fr} v_s - h_k (T_w - T_c) - \theta \phi (T_w^4 - T_c^4) \quad (2)$$

149

150 where τ_{fr} , v_s , h_k , T_w and T_c are friction stress in MPa, slip velocity $\text{mm}\cdot\text{s}^{-1}$, convective heat
 151 transfer coefficient in $\text{Wm}^{-2}\text{K}^{-1}$, wall (boundary) temperature in Kelvin, and ambient temperature
 152 in Kelvin, respectively. θ , ϕ and n are Stefan–Boltzmann constant in $\text{Wm}^{-2}\text{K}^{-4}$, emissivity and
 153 workpiece surface area in m^2 . Heat transfer coefficient was specified as a fixed value of $100 \text{ Wm}^{-2}\text{K}^{-1}$
 154 [20,35,42]. The thermal properties and boundary conditions presented in this paper are the
 155 same as those presented by the authors in a past paper [34].

156 Mechanical behaviour of the material during LFW is governed by the equilibrium equation
 157 expressed as [20,35]:

$$\rho \frac{\partial^2 u}{\partial t^2} = \nabla(\sigma) + \rho F \quad (3)$$

158

159 where u is material displacement vector, σ is stress tensor, F is body force vector per unit mass,
160 and t is time. The classic von Mises generalised model of the rate-dependent material is:

161

$$f(\sigma, \varphi) = \sigma_{eq} - \sigma_s(\bar{\varepsilon}^{pl}, \dot{\bar{\varepsilon}}^{pl}, T) = 0 \quad (4)$$

162

163 where σ_{eq} and σ_s are effective stress and material yield stress, respectively. The mechanical
164 boundary condition is pressure uniformly applied at the top surface of the stationary (i.e. top)
165 workpiece. This surface has constrained x-axis displacement and unconstrained y-axis
166 displacement to permit axial shortening (see Fig. 1). The oscillating (i.e. bottom) workpiece has x-
167 axis sinusoidal displacement, while displacement is constrained in the y-axis. The x-axis sinusoidal
168 displacement of the oscillating workpiece is controlled by:

169

$$x = A_0 \sin 2\pi f_0 t \quad (5)$$

170

171 where A_0 is the amplitude of oscillation (mm), f_0 is the frequency of oscillation (Hz) and t is the
172 instantaneous weld time, from 0.0 s to 5.0 s.

173

174 2.1.3 Constitutive material model and friction law

175 The elastic response of IN718 is assumed to be governed by Hooke's Law. The constitutive
176 material model employed in this study is the strain-compensated Arrhenius model expressed as
177 [20,35,41]:

178

$$\sigma_y = \frac{1}{\alpha(\varepsilon)} \ln \left\{ \left[\frac{\dot{\varepsilon}}{A(\varepsilon)} \exp\left(\frac{Q(\varepsilon)}{RT}\right) \right]^{\frac{1}{n(\varepsilon)}} + \left[\left[\frac{\dot{\varepsilon}}{A(\varepsilon)} \exp\left(\frac{Q(\varepsilon)}{RT}\right) \right]^{\frac{2}{n(\varepsilon)}} + 1 \right]^{\frac{1}{2}} \right\} \quad (6)$$

179

180 where σ_y is yield stress, $\dot{\varepsilon}$ is strain rate, T is absolute temperature, R is universal gas constant,
181 $Q(\varepsilon)$ is the deformation activation energy, and $\alpha(\varepsilon)$, $n(\varepsilon)$ and $A(\varepsilon)$ are material constants. They
182 are respectively expressed as polynomial functions of deformation strain as:

183

$$\alpha(\varepsilon) = B_0 + B_1\varepsilon + B_2\varepsilon^2 + B_3\varepsilon^3 + B_4\varepsilon^4 + B_5\varepsilon^5 \quad (7)$$

$$\begin{aligned}
n(\varepsilon) &= C_0 + C_1\varepsilon + C_2\varepsilon^2 + C_3\varepsilon^3 + C_4\varepsilon^4 + C_5\varepsilon^5 \\
Q(\varepsilon) &= D_0 + D_1\varepsilon + D_2\varepsilon^2 + D_3\varepsilon^3 + D_4\varepsilon^4 + D_5\varepsilon^5 \\
\ln A(\varepsilon) &= F_0 + F_1\varepsilon + F_2\varepsilon^2 + F_3\varepsilon^3 + F_4\varepsilon^4 + F_5\varepsilon^5
\end{aligned}$$

184

185 The coefficients of polynomial functions for the alloy material can be found in the research [40].

186 In this study, friction behaviour is represented by a plastically deformable friction pair
187 implemented by using the ‘surface-to-surface explicit’ friction contact behaviour. The magnitude
188 of contact pressure was computed in the thermomechanical modelling during LFW. Penalty
189 tangential workpiece interaction was specified for the transmission of shear stresses across the
190 contacting surfaces [7,34]. The friction coefficient depends on sliding velocity, friction interface
191 temperature, and contact pressure. A modified Coulomb’s friction law has been previously
192 employed for the target alloy IN718 given as [41]:

193

$$\mu = ap_f^b T^c \exp(dv_s) \quad (8)$$

194

195 where p_f is contact friction pressure, v_s is sliding velocity, and T is interface temperature between
196 the contacting friction surfaces. The constants a, b, c , and d are specified as 0.12, -0.233 , 0.471,
197 and -0.739 , respectively [41]. Maximum frictional stress τ_{fr} is limited by the strain rate and
198 temperature-dependent yield stress σ_y of IN718 material expressed as [20,41]:

199

$$\tau_{fr} = \min\left(\mu p_f, \frac{\sigma_y}{\sqrt{3}}\right) \quad (9)$$

200

201 **2.2 Microstructural model for DRX of γ grain during LFW**

202 LFW typically involves a very high heating rate and high weld temperature within a relatively
203 short time, which may significantly affect the size of primary γ grains due to dynamic
204 recrystallisation [17]. In this study, the DRX of γ grains during LFW was formulated by using the
205 empirical JMAK model [30,46,51]. The volume fraction of recrystallised γ grains X_{DRX} is given
206 as [30]:

207

$$X_{DRX} = 1 - \exp\left[-\ln 2 \left(\frac{\varepsilon - \varepsilon_c}{\varepsilon_{0.5} - \varepsilon_c}\right)^{n_d}\right] \quad ; \quad (\varepsilon \geq \varepsilon_c) \quad (10)$$

208

209 where ε is current plastic strain, ε_c is critical plastic strain for DRX initiation, $\varepsilon_{0.5}$ is strain for 50%
210 volume fraction of DRX, and n_d is the Avrami constant.

211 ε_c and $\varepsilon_{0.5}$ are expressed as [30]:

212

$$\varepsilon_c = \varepsilon_{c1} Z^{n_{c1}} \quad (11)$$

213

$$\varepsilon_{0.5} = \varepsilon_{b1} Z^{n_{b1}} \quad (12)$$

214

$$Z(\varepsilon) = \dot{\varepsilon} \exp \left[\frac{Q}{RT} \right] \quad (13)$$

215

216 where ε_{c1} , ε_{b1} , n_{b1} , n_{c1} are material constants taken from [30]. Zener-Hollomon parameter Z is
 217 expressed as the relation between weld temperature T and plastic strain rate $\dot{\varepsilon}$ during LFW [46,58].
 218 Equation 10 follows a strain based DRX initiation criteria, such that DRX takes place when the
 219 current plastic strain reaches or exceeds the critical plastic strain. Geng et al. applied Eqs. 10 to 13
 220 within the temperature range (1213 – 1453 K), which is higher than the γ' and δ equilibrium solvus
 221 temperatures of 1172 K and 1283 K [30,34]. In this study, the critical temperature for onset of
 222 DRX is assumed to be 1213 K. The material constants in relation to DRX of γ grains of IN718
 223 alloy were sourced from Geng et al. [11,30].

224 X_{DRX} is predicted according to an incremental form of the JMAK model that is activated by plastic
 225 strain ε expressed as [30,46]:

226

$$dX_{DRX} = \exp \left[-\ln 2 \left(\frac{\varepsilon - \varepsilon_c}{\varepsilon_{0.5} - \varepsilon_c} \right)^{n_d} \right] \left[n_d \ln 2 \left(\frac{\varepsilon - \varepsilon_c}{\varepsilon_{0.5} - \varepsilon_c} \right)^{n_d - 1} \right] \left(\frac{1}{\varepsilon_{0.5} - \varepsilon_c} \right) d\varepsilon \quad (14)$$

227

228 The volume fraction of recrystallised grains can be updated by using the equation [46,58]:

229

$$X_{DRX(t)} = X_{DRX(t-1)} + dX_{DRX(t)} \quad (15)$$

230 where $X_{DRX(t)}$, $X_{DRX(t-1)}$, and $dX_{DRX(t)}$ are the current step volume fraction, previous step volume
 231 fraction, and increment in volume fraction of recrystallised grains, respectively. The size and
 232 dynamically recrystallised volume fraction of IN718 γ grains prior to DRX were set to be 20 μm
 233 and 0.01%, respectively [30]. The dynamically recrystallised grain size d_{DRX} in μm can be
 234 computed using three different regimes of plastic strain rate based on Zener-Hollomon parameter
 235 Z as follows [11]:

236

$$d_{DRX} = -g_{l1} \ln Z + g_{c1} \quad ; \quad (\dot{\varepsilon} < 0.1 \text{ s}^{-1}) \quad (16)$$

237

$$d_{DRX} = -g_{l2} \ln Z + g_{c2} \quad ; \quad (0.1 \text{ s}^{-1} < \dot{\epsilon} < 10 \text{ s}^{-1}) \quad (17)$$

$$d_{DRX} = -g_{l3} \ln Z + g_{c3} \quad ; \quad (\dot{\epsilon} > 10 \text{ s}^{-1}) \quad (18)$$

238

239

240 where g_{c1} , g_{c2} , g_{c3} , g_{l1} , g_{l2} , and g_{l3} are material constants, ($\dot{\epsilon} < 0.1 \text{ s}^{-1}$) for low strain rate
 241 regimes, ($0.1 \text{ s}^{-1} < \dot{\epsilon} < 10 \text{ s}^{-1}$) for medium strain rate regimes, and ($\dot{\epsilon} > 10 \text{ s}^{-1}$) for high
 242 strain rate regimes, and their values were taken from Geng et al. [11]. The average grain size
 243 D_{ave} was calculated by using a weighted average of the recrystallised grain size d_{DRX} and non-
 244 recrystallised grain size $D_{ave(t-1)}$ as [46]:

245

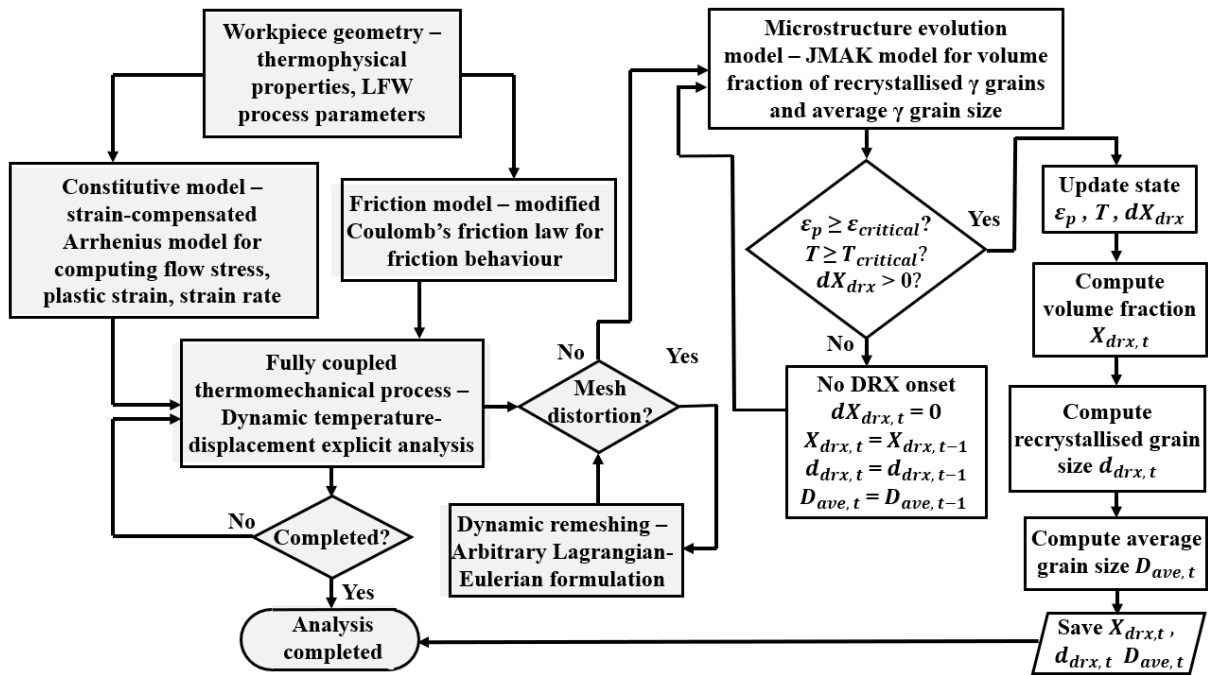
$$D_{ave(t)} = d_{DRX} (X_{DRX}) + D_{ave(t-1)} (1 - X_{DRX}) \quad (19)$$

246 where (t) and $(t - 1)$ are the current and previous computational time steps.

247

248 **2.3 Model integration**

249 Figure 2 presents a flowchart showing how the integrated multiphysics computational modelling
 250 works as well as the sequential coupling between the thermomechanical submodel and the
 251 microstructural submodel. For each computational time step, the thermomechanical and
 252 microstructural submodels are solved simultaneously. State variables such as temperature, plastic
 253 strain, and strain rate are computed by Abaqus/Explicit solver during the explicit dynamic
 254 temperature-displacement coupled analysis of LFW process. The VUHARD subroutine captures
 255 the computational results of state variables for use in the microstructural model. Then Eqs. 10 to
 256 19 are solved by Abaqus/Explicit in conjunction with related Abaqus/Explicit VUHARD code. In
 257 this sequential coupling between the thermomechanical sub-model and the microstructural sub-
 258 model, it is assumed that the DRX process of γ grains does not influence the thermomechanical
 259 responses of IN718 during LFW.



261

262 **Fig. 2** Flowchart of the integrated multiphysics computational modelling for LFW. The grey-

263 coloured shapes represent the thermomechanical submodel and the white-coloured shapes

264 represent the microstructural submodel in the VUHARD subroutine

265

266 **2.4 Process parameters of LFW and material properties**

267 In total, 20 different process parameter sets for LFW were defined (see Table 1) based on three

268 key LFW process parameters, which are friction pressure p_f , oscillating amplitude A_0 , and269 oscillating frequency f_0 . The average rubbing velocity v_r is determined from the oscillating270 amplitude A_0 and oscillating frequency f_0 using $v_r = 4A_0f_0$ [1]. The 20 different LFW setups

271 were used as the background of computational modelling for systematically predicting the

272 influence of process parameters on weld temperature, γ grain size, and volume fraction of273 recrystallised γ grains during IN718 LFW.

274

275

Table 1 Process parameters applied in LFW computational modelling

Number of weld	Friction pressure p_f (MPa)	Oscillating frequency f_0 (Hz)	Oscillating amplitude A_0 (mm)	Average rubbing velocity v_r (mm/s)
J1	100	15	2.5	150
J2	100	20	2.5	200
J3	100	40	3.3	528

J4	200	20	3.3	264
J5	200	25	2.9	290
J6	200	40	2.5	400
J7	200	40	3.3	528
J8	300	15	2.5	150
J9	300	20	3.3	264
J10	300	25	2.9	290
J11	300	30	2.9	348
J12	400	15	2.5	150
J13	400	25	2.9	290
J14	400	20	3.3	264
J15	400	30	2.9	348
J16	500	20	3.3	264
J17	500	25	2.9	290
J18	500	30	2.5	300
J19	600	15	2.5	150
J20	600	20	2.5	200

276

277 The material properties of IN718 are assumed to be isotropic. The IN718 thermophysical
 278 properties used in the model were taken from [20]. Other material properties and LFW input
 279 process parameters can be found in Table 2. The chemical composition of IN718 is Ni-0.5Al-
 280 19.0Cr-18.5Fe-3.0Mo-5.1Nb-0.9Ti-0.04C in mass percentage [10].

281

282 **Table 2** Other related process, material and modelling parameters used in the modelling [20]

<i>Thermomechanical input parameter</i>	<i>Value</i>
Room temperature (K)	298
Liquidus temperature of alloy (K)	1633
Thermal conductivity λ (W/m/K)	$0.016T + 16.668$
Specific heat capacity c_p (J/kg/K)	$0.33T + 452.09$
Expansion α_w (1/K)	$4 \times 10^{-9}T + 10^{-5}$
Density ρ (kg/m ³)	8420
Elastic modulus E (MPa)	221000

Poisson's ratio ν	0.3
Inelastic heat fraction	0.9
Heat partition coefficient	0.5
Friction energy change to heat	0.9
Mean friction coefficient	0.01–0.60
Shear stress limit (MPa)	60–100

283

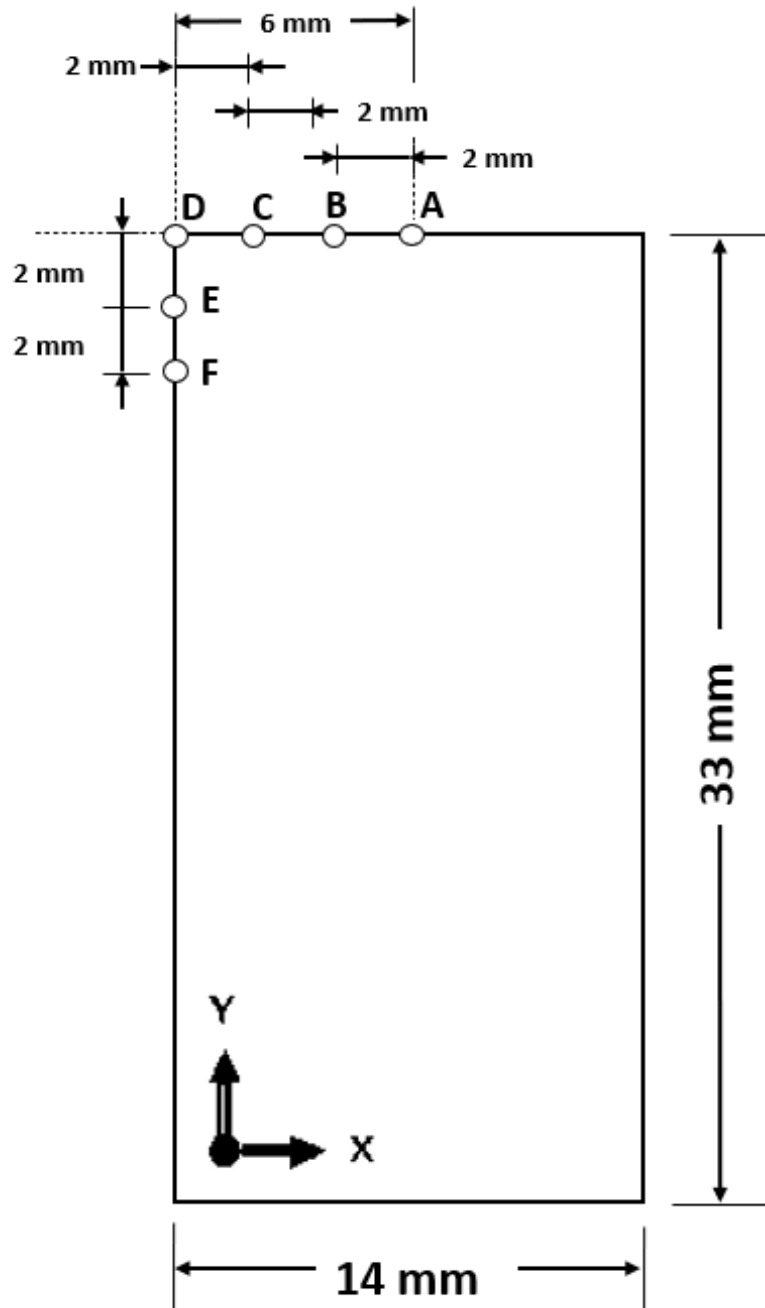
284 The initial volume fraction of recrystallised γ grains before the start of LFW (which is also its
285 lower limit) is set to 0.01% (for no recrystallised grains at all) and the upper limit of volume
286 fraction of recrystallised γ grains is set to 99.99% (for fully recrystallised material). This will avoid
287 numerical singularities, whilst having a very limited influence on the modelling results. Before the
288 start of LFW, the size of non-recrystallised γ grains is assumed to be 20 μm and the size of
289 recrystallised γ grain is assumed to be 3 μm .

290

291 **3 Results and discussion**

292 **3.1 Temperature and plastic strain evolution**

293 Figure 3 shows six sampling points A, B, C, D, E, and F (not drawn to scale) on the friction
294 interface and the left side of the bottom workpiece at the start of welding. The sampling points are
295 2 mm apart before welding starts and can get displaced further from one another during LFW
296 because of the deformation of the weld. Line profiles of some modelling output parameters are
297 presented for only the bottom workpiece considering that thermal histories and microstructural
298 evolution are generally mirrored in both workpieces across the friction interface [11,20,35].
299 Thermomechanical model verification in relation to weld temperature, axial shortening, and flash
300 shape has been previously presented by the authors in [33,34]. Thus, this study focuses primarily
301 on the analysis of the microstructural modelling results.



303

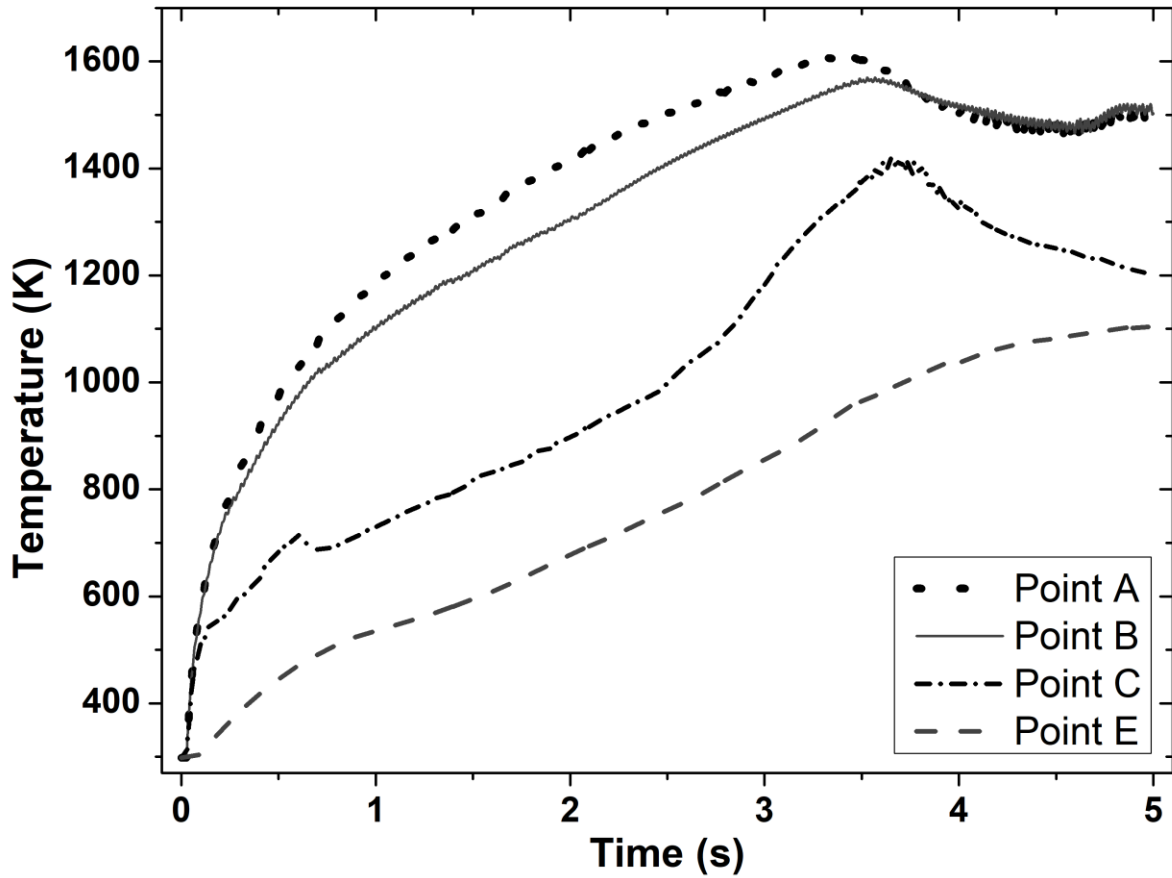
304 **Fig. 3** 2D geometry of the bottom workpiece of LFW and the position of six sampling points (A,
 305 B, C, D, E, and F) identified on the friction interface and left side of the bottom workpiece

306

307 Figures 4 and 5 show the computational modelling results of the evolution of temperature and
 308 plastic strain with time at sampling points A, B, C, and E (as shown in Fig. 3) for the LFW setup
 309 J13. LFW setup J13 was selected as the reference welding parameter set in this study to ensure

310 consistent comparison with the experimental results of Geng et al. (based on the same workpiece
311 dimension and weld configuration) and to achieve model verification [11]. Additionally, setups J1
312 to J20 were used to show other capabilities of the integrated computational model.

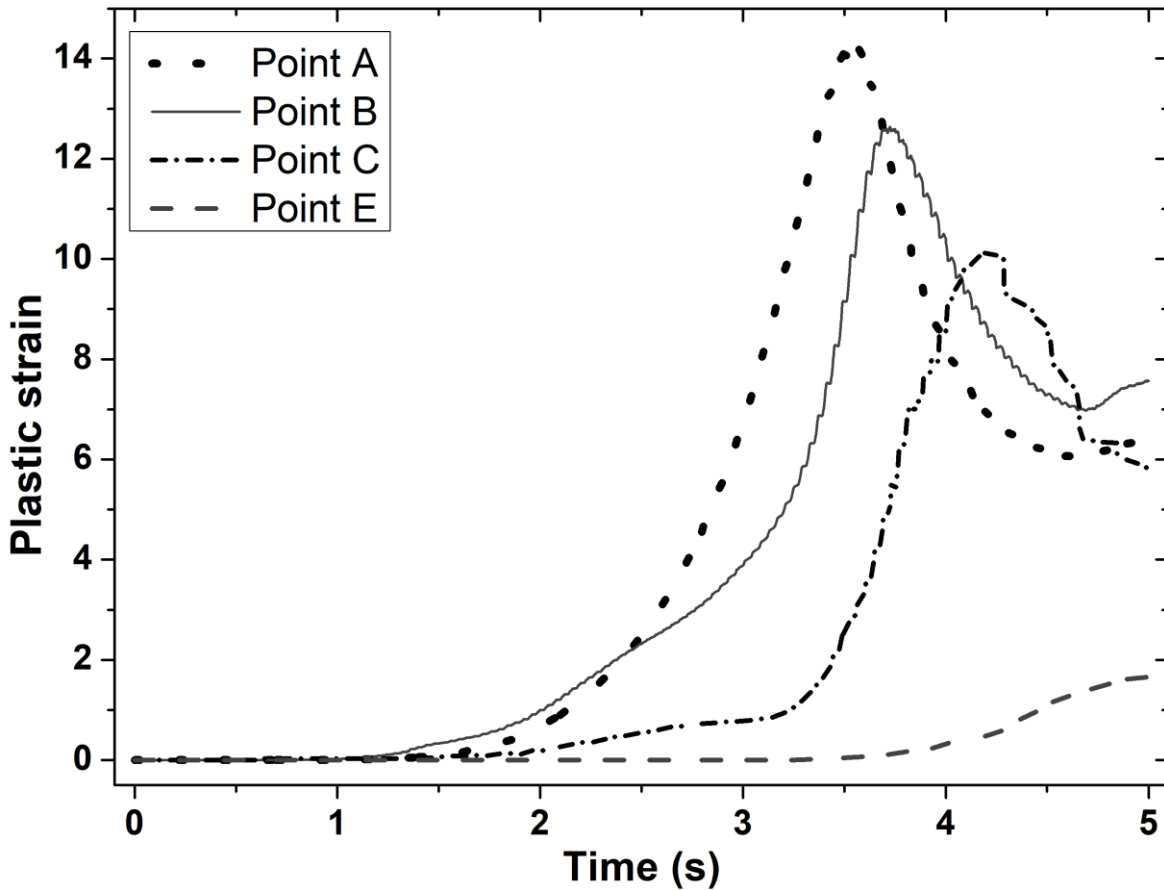
313



314

315 **Fig. 4** Temperature histories of sampling points A, B, C and E on the bottom workpiece for LFW
316 setup J13

317



318

319 **Fig. 5** Evolution of plastic strain with time at sampling points A, B, C and E on the bottom
 320 workpiece for LFW setup J13

321

322 In Fig. 4, the maximum temperature at sampling points A, B, C and E is 1610 K, 1570 K, 1420 K,
 323 and 1106 K, respectively. These maximum temperature levels are lower than the liquidus
 324 temperature of IN718 (~1633 K). At such elevated levels of temperature, the weld undergoes
 325 significant material softening, flash formation and extrusion at the friction interface of workpieces
 326 [8]. Sampling point A is shown to have the highest temperature; it is exactly at the mid-region of
 327 the friction interface. Sampling points B, C, and E show lower levels of temperature compared to
 328 sampling point A and these three points are further away from the mid-region of the friction
 329 interface. The maximum temperature was reached at 3.55 s, 3.53 s, and 3.65 s of welding for
 330 sampling points A, B and C, respectively, while the maximum temperature was reached at 5.00 s
 331 of welding for sampling point E. The evolution of temperature with time at different stages of the
 332 LFW process was well explained in the previous work of the authors [33,34]. Although
 333 temperature levels vary at different positions on the workpiece, it is the highest at the centre of the
 334 friction interface and becomes increasingly lower away from the centre [20,33].

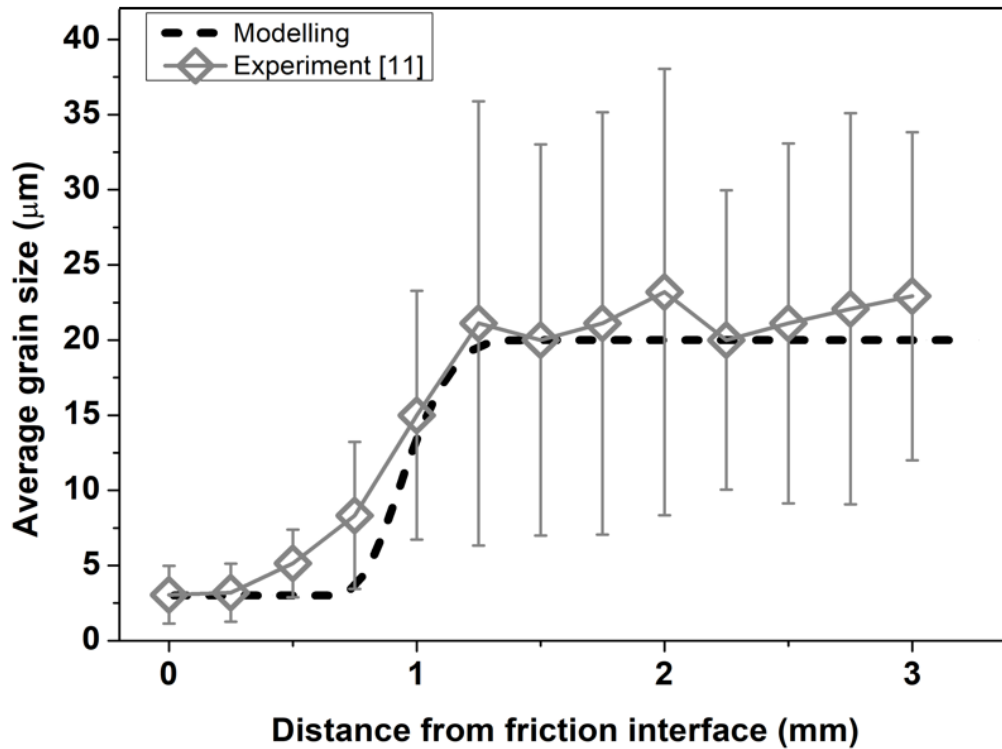
335 In Fig. 5, the maximum plastic strain at sampling points A, B, C, and E is 14.29, 12.64, 10.14, and
 336 1.66, respectively, which was reached at welding time 3.53 s, 3.73 s, 4.21 s, and 5.00 s,

337 respectively. These maximum plastic strains were reached in the equilibrium and extrusion stages
338 of LFW, as explained in the author's previous work [33]. However, only sampling points A, B,
339 and C are displaced considerably. Similar to the varying levels of temperature, the plastic strain
340 level varies at different positions on the bottom workpiece. It reached a maximum level at the
341 centre of the friction interface and becomes increasingly lower away from the centre. Other
342 researchers found similar variations in the plastic strain at different regions of the workpieces
343 during LFW [20,35,42]. The temperature histories and plastic strain evolution (see figures 4 and
344 5), as well as strain rate, are important thermomechanical modelling results, which are used as
345 inputs of microstructural modelling of DRX process of γ grains during LFW.

346

347 **3.2 Microstructural model verification and evolution of γ grains**

348 In order to verify the integrated model in terms of modelling the DRX of γ grains during LFW of
349 IN718, the computational modelling results of this paper are compared with related experimental
350 results of Geng et al. as shown in Fig. 6 [11]. Specifically, the LFW of IN718 was completed for
351 5 s in the modelling of the authors as well as in the experimental research of Geng et al. according
352 to the setup J13 [11]. The average size of γ grain is characterised along a sampling path L—M of
353 the weld. It can be seen in Fig. 6 that the modelling result of average γ grain size agrees with related
354 experimental results, especially beyond 1-mm distance from the friction interface. This proves that
355 the integrated computational model reasonably predicted the evolution of γ grain size due to DRX
356 during LFW of IN718. Besides verifying the model using LFW setup J13, other capabilities of the
357 integrated computational model are shown using LFW setups J1 to J20 in subsequent sections of
358 this paper.

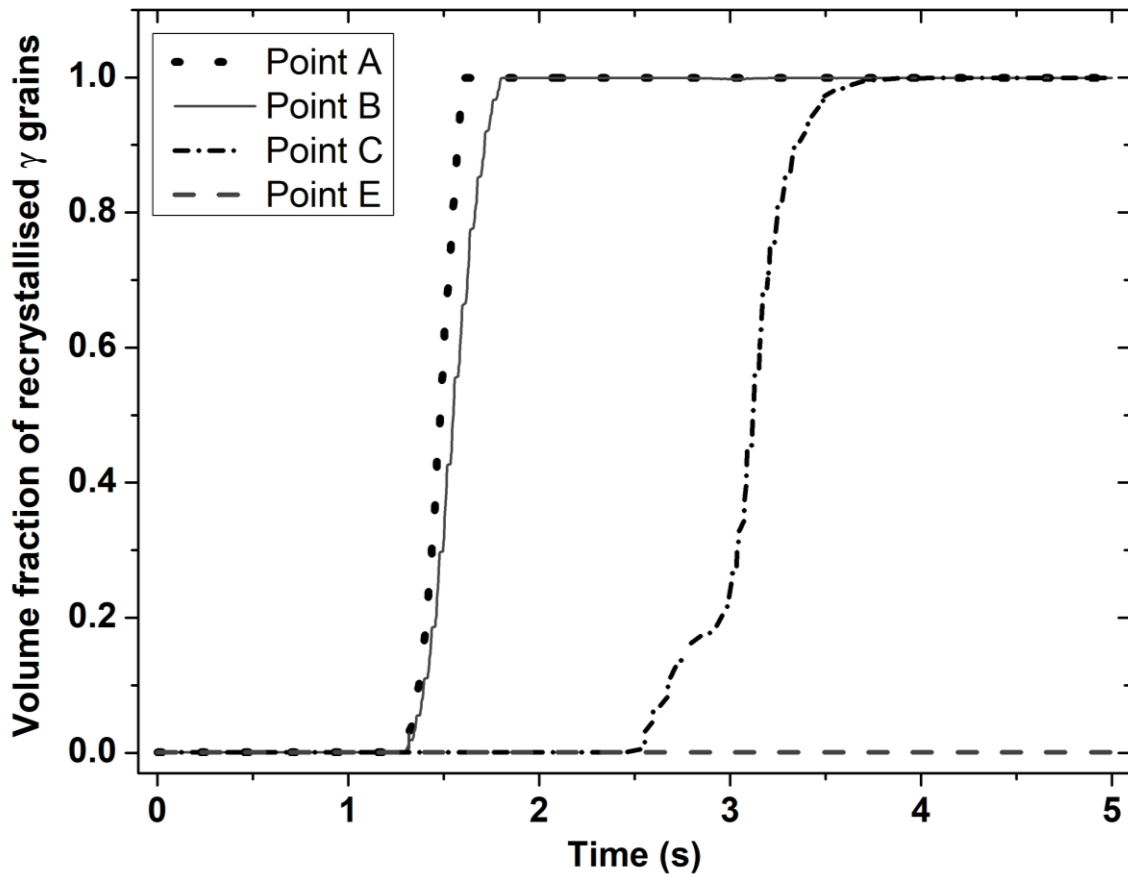


360

361 **Fig. 6** Comparison of the experimentally measured result of average γ grain size (Experiment) of
 362 Geng et al. with computational modelling results of average γ grain size (Modelling) in this study
 363 for path L–M of LFW setup J13 at 5.0 s of welding [11]

364

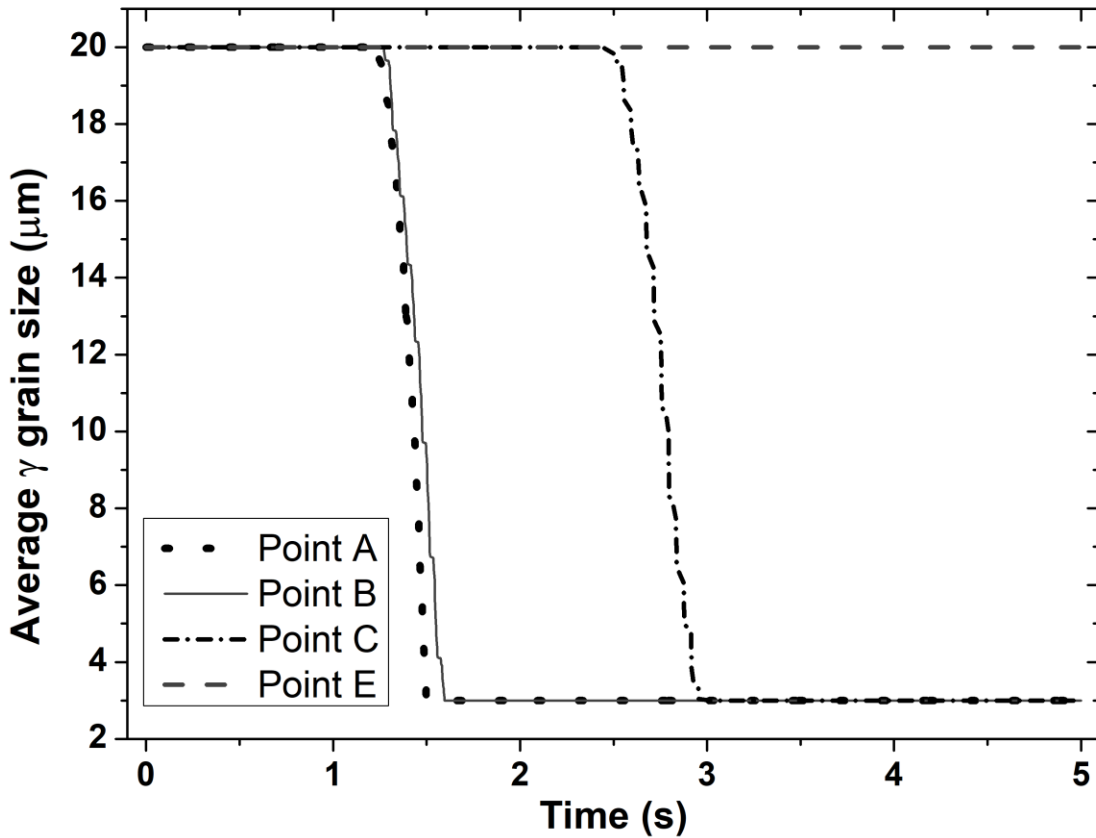
365 Figures 7 and 8 show the temporal evolution of volume fraction of dynamically recrystallised γ
 366 grains and the temporal evolution of average γ grain size at sampling points A, B, C, and E of the
 367 bottom workpiece for LFW setup J13. In Fig. 7, γ grains get fully recrystallised at welding time of
 368 1.9 s, 2.7 s, and 3.4 s at sampling points A, B, and C, while the volume fraction of recrystallised γ
 369 grains evolves between 0.01 and 99.99%. Comparing Fig. 7 with Fig. 8, it can be seen that the
 370 increase in the volume fraction of recrystallised γ grains corresponds to a decrease in the average
 371 size of γ grains. It indicates that the DRX process refines γ grains during LFW of IN718 [30,51,59].
 372 At sampling point E, the volume fraction of recrystallised γ grains as well as the average size of γ
 373 grains did not change during LFW because the computationally predicted maximum temperature
 374 of the material (1106 K) during LFW at sampling point E is below the critical temperature (1213
 375 K) for the onset of DRX.



377

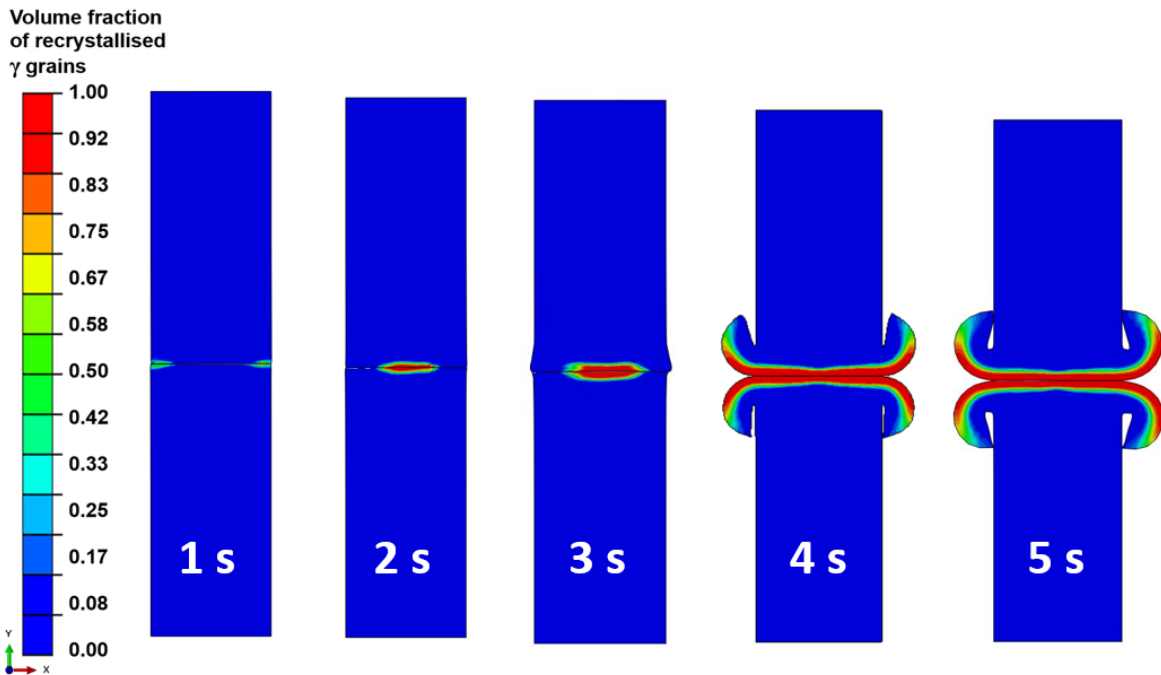
378 **Fig. 7** Temporal evolution of volume fraction of recrystallised γ grains at sampling points A, B,
379 C and E of the bottom workpiece for LFW setup J13

380



381
 382 **Fig. 8** Temporal evolution of average γ grain size at sampling points A, B, C and E of the bottom
 383 workpiece for LFW setup J13

384
 385 Figure 9 shows the evolution of the spatial distribution of volume fraction of recrystallised γ grains
 386 during the LFW process, in the overall weld for setup J13. At 1.0 s of welding, the volume fraction
 387 has not changed in the weld because the maximum temperature is still below the critical
 388 temperature of 1213 K for the onset of DRX. At 2.0 s of welding, the maximum volume fraction
 389 has increased to 0.83, around the friction interface. Up to 3.0 s of welding time, the maximum
 390 volume fraction has further increased to 1.00 at the friction interface and all γ grains become
 391 recrystallised in the close vicinity of a very significantly deformed friction interface. The volume
 392 fraction is 1.00 up to 5.0 s of LFW. Overall, because high temperature and significant plastic
 393 deformation of material only happen in the close vicinity of the friction interface, full
 394 recrystallisation can only happen in a very narrow zone that is within 1.5 mm of each workpiece
 395 relative to the friction interface, which is approximately the red zone as shown in Fig. 9.

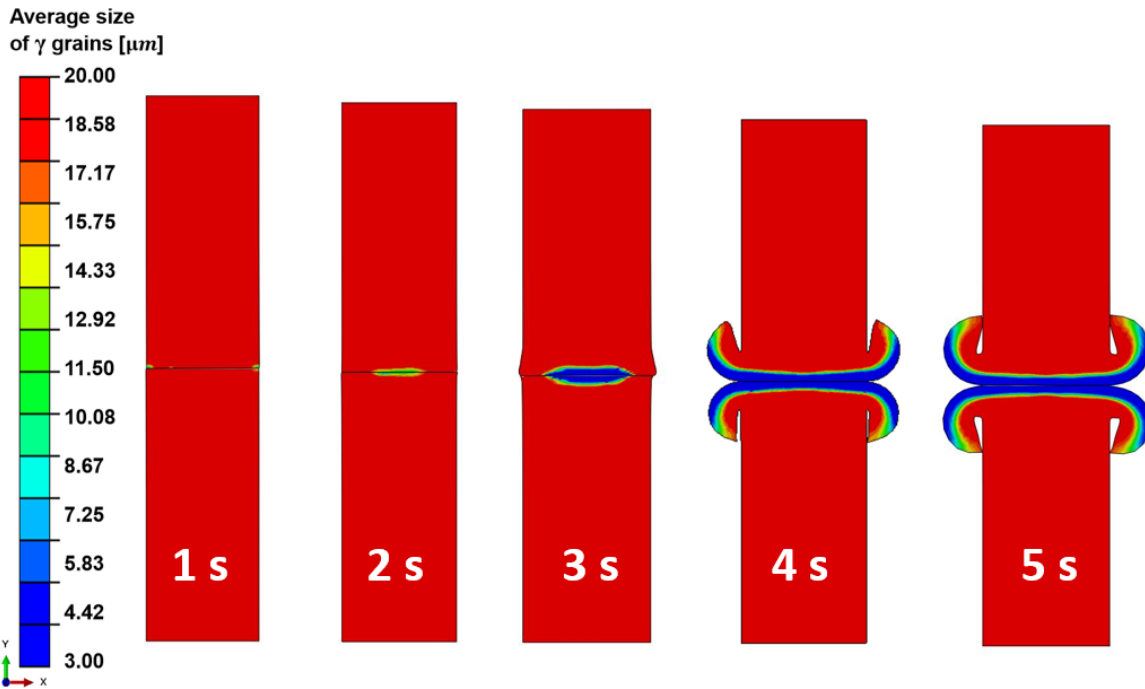


397

398 **Fig. 9** Temporal evolution of spatial distribution of volume fraction of recrystallised γ grains of
 399 the weld during LFW process for setup J13 where $p_f = 400$ MPa, $f_0 = 25$ Hz and $A_0 =$
 400 2.9 mm

401

402 Figure 10 shows the temporal evolution of the spatial distribution of average γ grain size for setup
 403 J13. At 1.0 s of welding, the average grain size has not changed in the weld because the maximum
 404 temperature is below the critical temperature of 1213 K for the onset of DRX and DRX has not
 405 started yet. At 2.0 s of welding, the average γ grain size has decreased from 20.0 to 14.3 μm near
 406 the centre of the friction interface. It further decreases to 4.4 μm at the centre of friction interface
 407 at welding time of 3.0 s. At 4.0 s of welding, the average γ grain size is 3.0 μm at the friction
 408 interface, while γ grains are still relatively larger away from the friction interface. At 5.0 s of
 409 welding, the average γ grain size is 3.0 μm along the entire significantly deformed friction
 410 interface. However, such a fine grain region exists within 1.5 mm relative to the friction interface
 411 of each workpiece. Away from the friction interface, the average γ grain size continuously
 412 increases from 3.0 to 20.0 μm , as shown in Fig. 6 and Fig. 10.



414

415 **Fig. 10** Temporal evolution of the spatial distribution of average γ grain size of the weld during
 416 LFW process for setup J13 where $p_f = 400$ MPa, $f_0 = 25$ Hz and $A_0 = 2.9$ mm

417

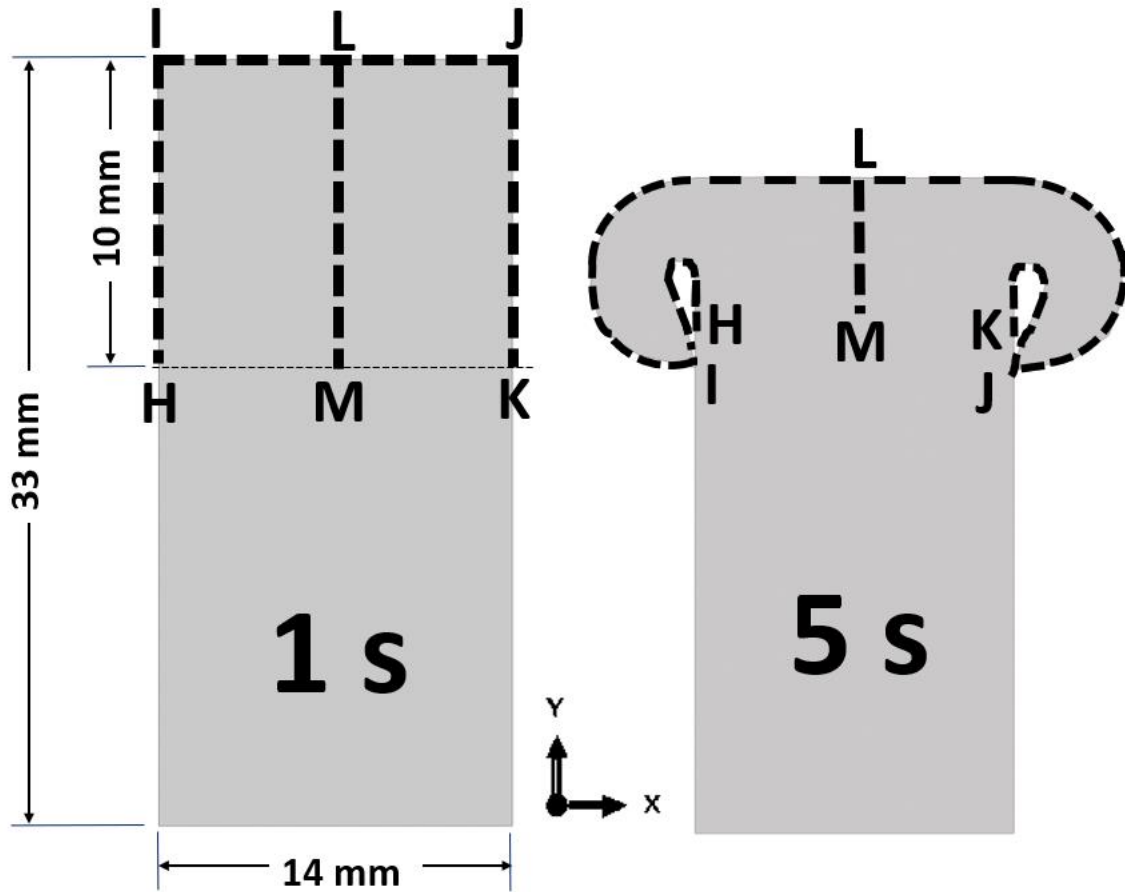
418 By comparing the modelling results shown in Fig. 9 and Fig. 10, it can be seen that very significant
 419 dynamic recrystallisation very rapidly happened in the weld during LFW but only within a very
 420 limited volume of material that is within 1.5 mm relative to the friction interface. Within this
 421 region, γ grains become fully recrystallised since approximately 5.0 s of LFW. The fully
 422 recrystallised material has a relatively small average γ grain size.

423

424 3.3 LFW process parameter optimisation

425 3.3.1 Relationship between average γ grain size, volume fraction of recrystallised γ grains 426 and temperature of weld

427 The modelling results of such as volume fraction of recrystallised grains, average γ grain size and
 428 weld temperature are analyzed along path L—M (10 mm long) and path H—I—J—K (34 mm long)
 429 as shown in Fig. 11, at the surface of the bottom workpiece based on LFW setup J13. There are 53
 430 and 157 sampling points on paths L—M and H—I—J—K. Axial shortening and flash formation of
 431 weld can cause the length of path L—M to reduce considerably while the length of path H—I—J—K
 432 increases considerably during LFW process (see Fig. 11). The direction of path L—M in this paper
 433 is from L to M and that of path H—I—J—K is from H to I, I to J and J to K. These paths are data
 434 sampling paths, which are employed in this paper only for data analysis purposes. They do not
 435 imply any partition of the workpiece.



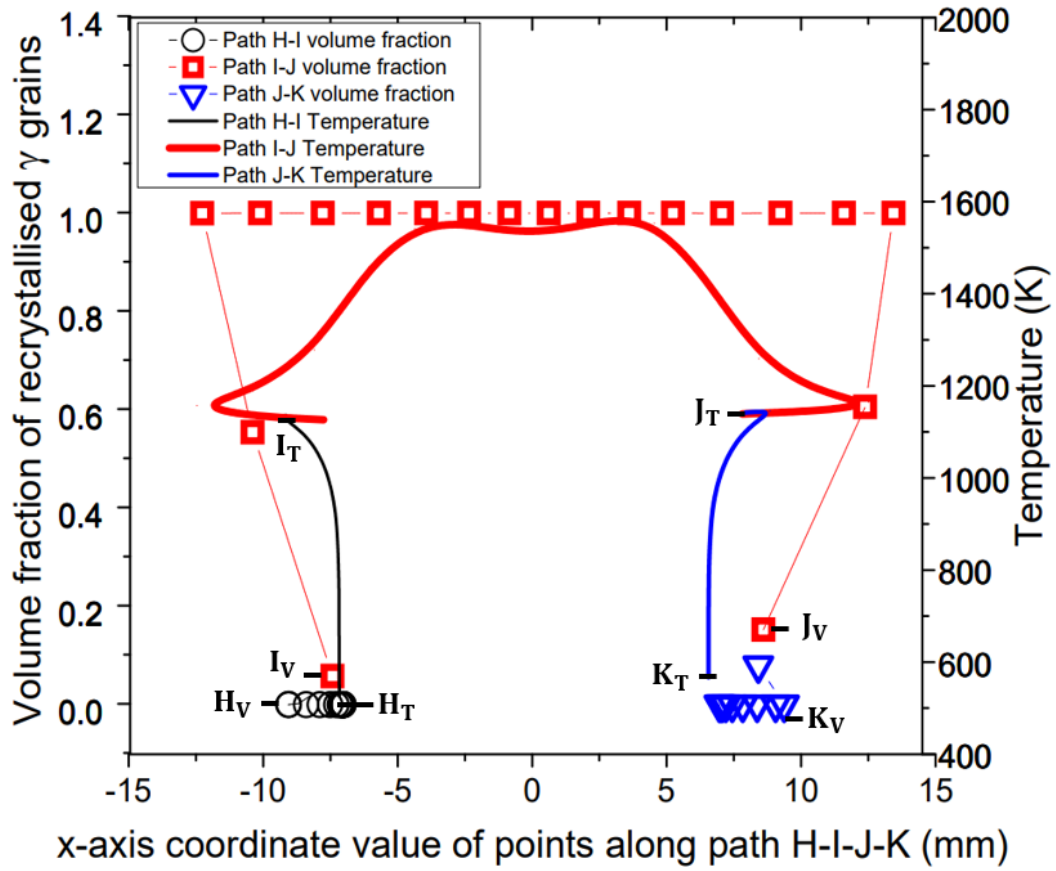
437

438 **Fig. 11** Data sampling paths L–M (10 mm long) and H–I–J–K (34 mm long) at the surface of
 439 the bottom weld based on LFW setup J13

440

441 Figure 12(a) and 12(b) show the profiles of temperature (identified with subscript ‘T’), volume
 442 fraction of recrystallised γ grains (identified with subscript ‘V’) and average γ grain size (identified
 443 with subscript ‘G’) along each path H–I, I–J, and J–K for LFW setup J13 at 5.0 s of welding. The
 444 centre of friction interface of the bottom workpiece is at $x = 0$ mm according to the Cartesian
 445 coordinates (X - Y axes) of the 2D model.

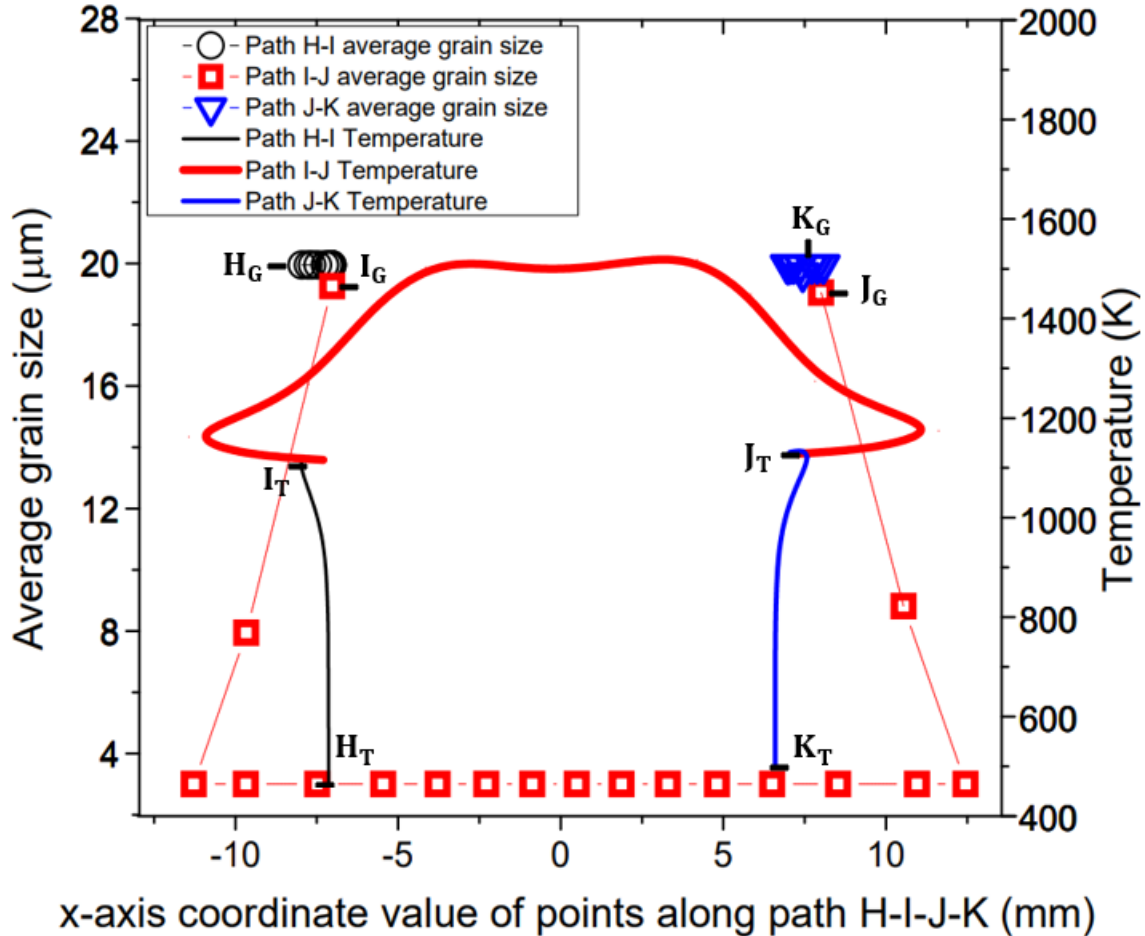
446



447

448

(a)



450

451

(b)

452

453

454

455

Fig. 12 Computational modelling results of profile of (a) volume fraction of recrystallised γ grains and temperature (b) average size of γ grains and temperature along paths H–I, I–J and J–K for LFW setup J13, with subscript ‘V’ for volume fraction, ‘T’ for temperature and subscript ‘G’ for grain size

456

457

458

459

460

461

462

463

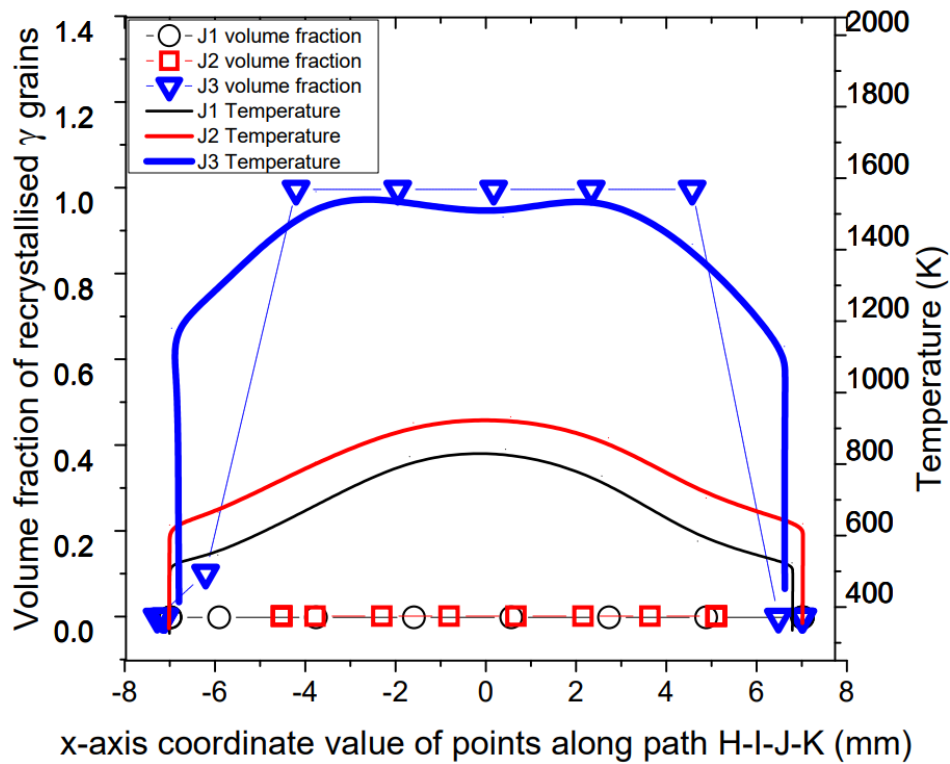
464

In figure 12(a) and 12(b), the profiles of volume fraction of recrystallised γ grains and average γ grain size, along paths H–I and J–K for setup J13 show that no DRX (and corresponding grain refinement) happened at the side surface of weld (along path H–I and path J–K) because the maximum temperature (1116 K) is considerably below the critical temperature for onset of DRX (1213 K). However, for the profile along path I–J, which includes the friction interface of the weld, γ grains are fully recrystallised resulting in significant grain refinement up to $x = \pm 5.4$ mm relative to the centre of friction interface. This is due to the significantly elevated level of temperature along path I–J.

465 To achieve process parameter optimisation, the modelling results for setups J1 to J20 are herein
 466 presented following the same relationships as in setup J13 by relating the average γ grain size,
 467 volume fraction of recrystallised γ grains and temperature of weld. Figure 13(a) – 13(g) and 14(a)
 468 – 14(g) illustrate the profiles of volume fraction of recrystallised γ grains, average γ grain size,
 469 and temperature along the path H–I–J–K at 5.0 s of welding for all 20 different LFW setups. The
 470 20 different LFW setups resulted in varying levels of weld temperature and microstructural
 471 evolution in terms of recrystallisation and grain refinement, as presented in this section and
 472 subsequent sections of this paper.

473 Figures 13(a) and 14(a) show that no DRX of γ grains occurred during LFW process of setup J1
 474 and J2, because the maximum temperature is 850 K and 933 K, which is well below the critical
 475 temperature for onset of DRX (1213 K). For LFW setup J3, γ grains are fully recrystallised and
 476 refined within $x = \pm 5.8$ mm relative to the centre of weld along the path H–I–J–K. The
 477 maximum temperature of setup J3 is 1585 K, which is below the IN718 liquidus temperature of
 478 1633 K; hence, no remelting happened at the friction interface of weld.

479

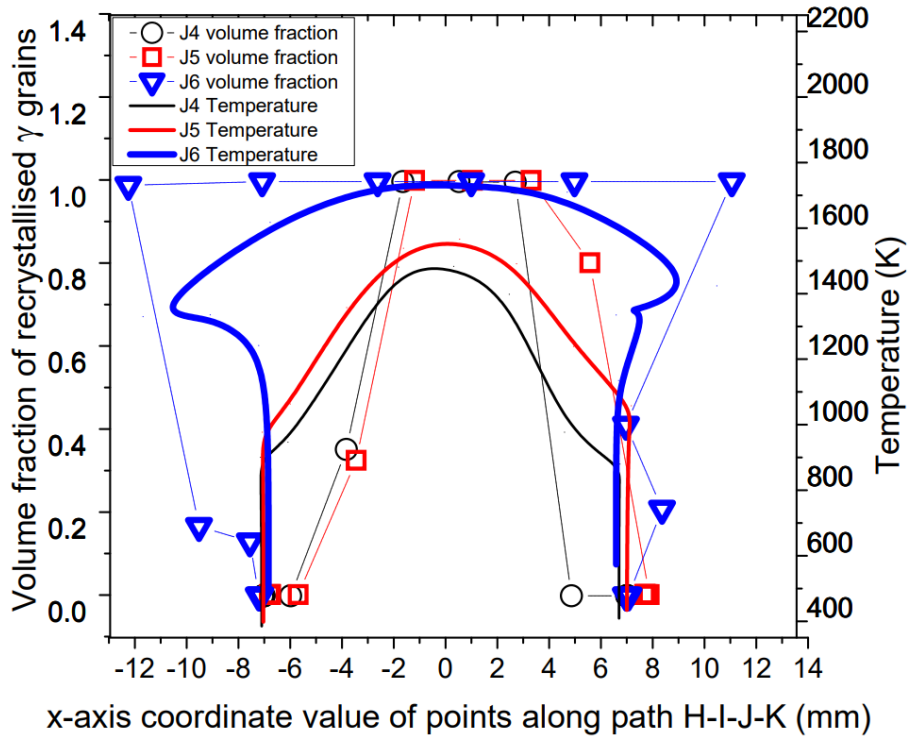


480

481

482

(a)

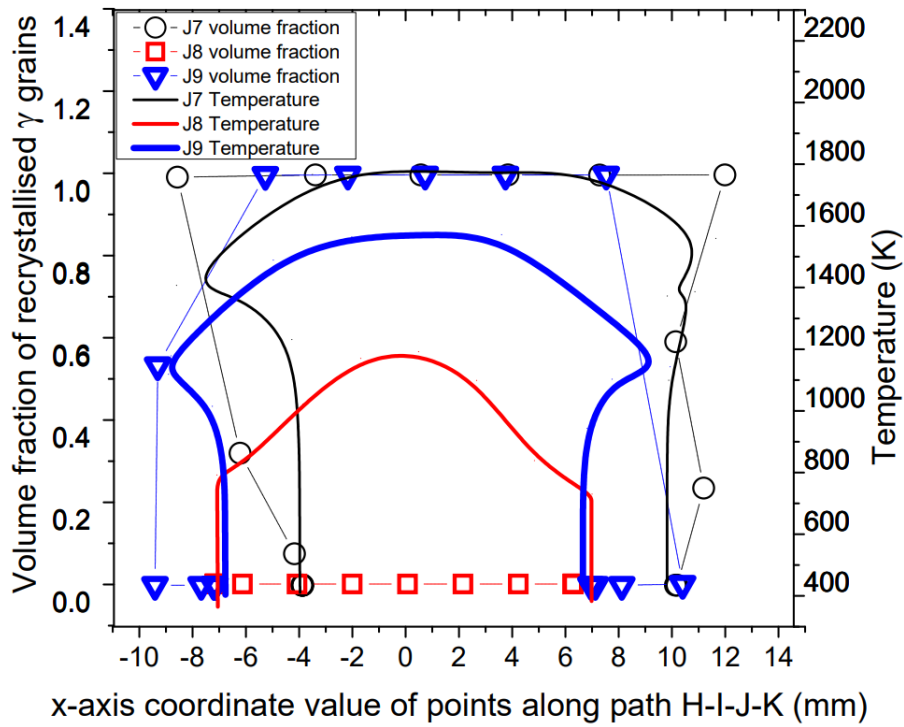


483

484

485

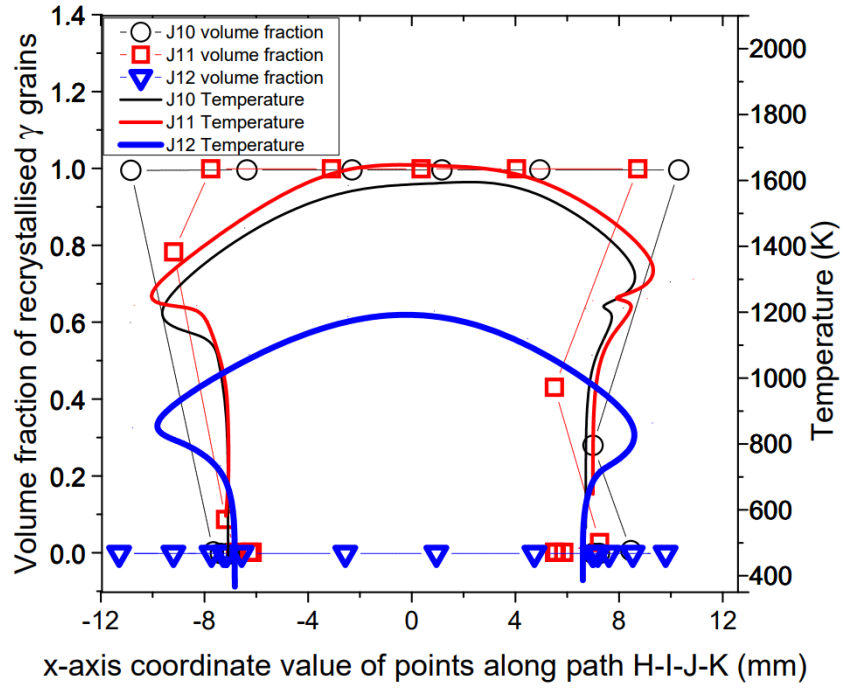
(b)



486

487

(c)

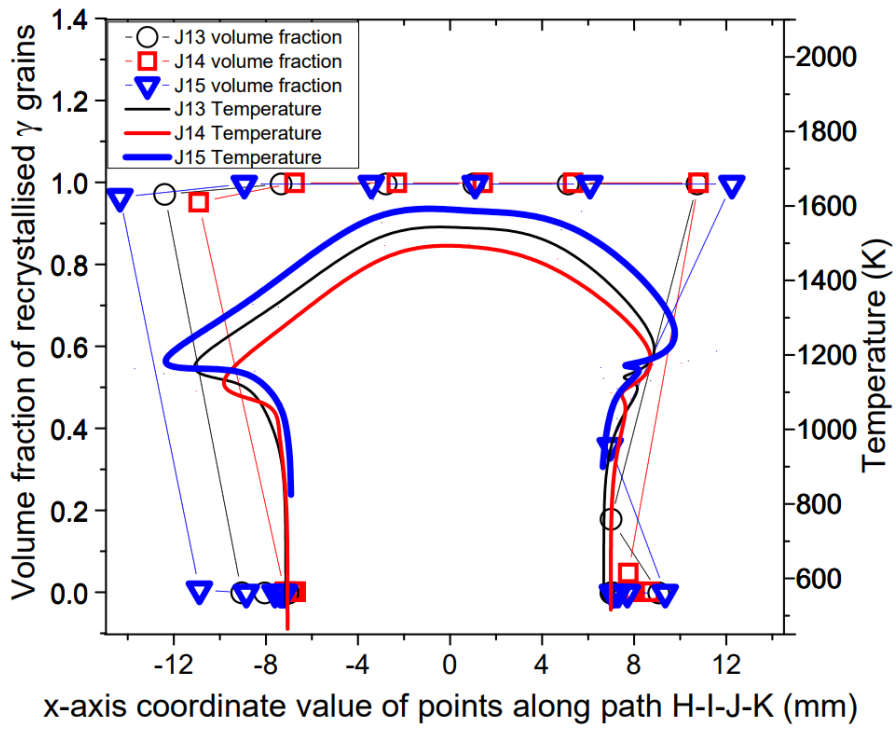


489

490

491

(d)

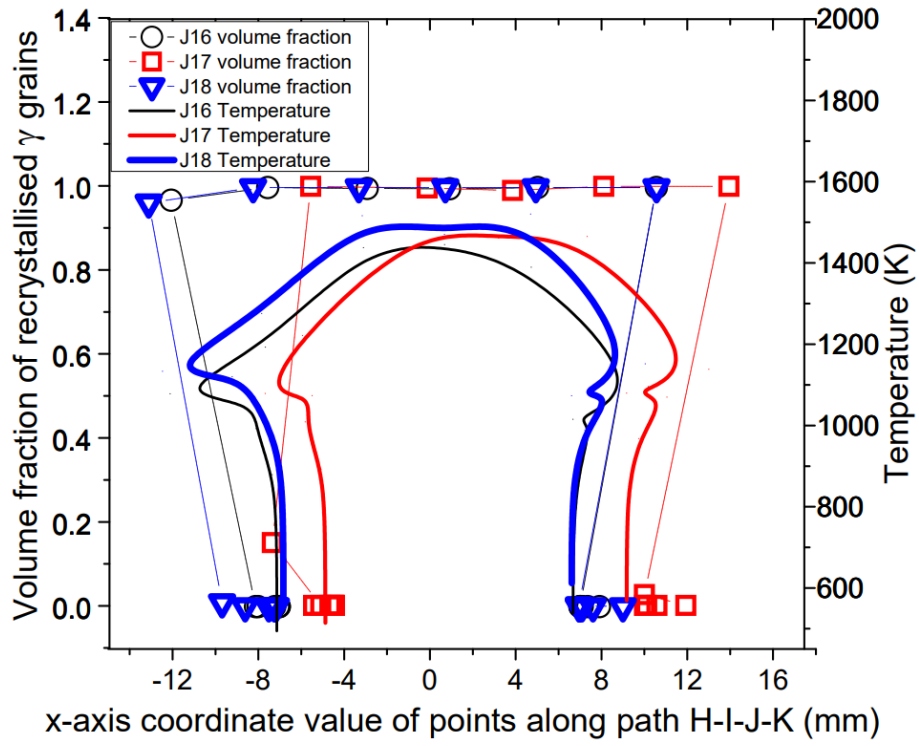


492

493

(e)

494

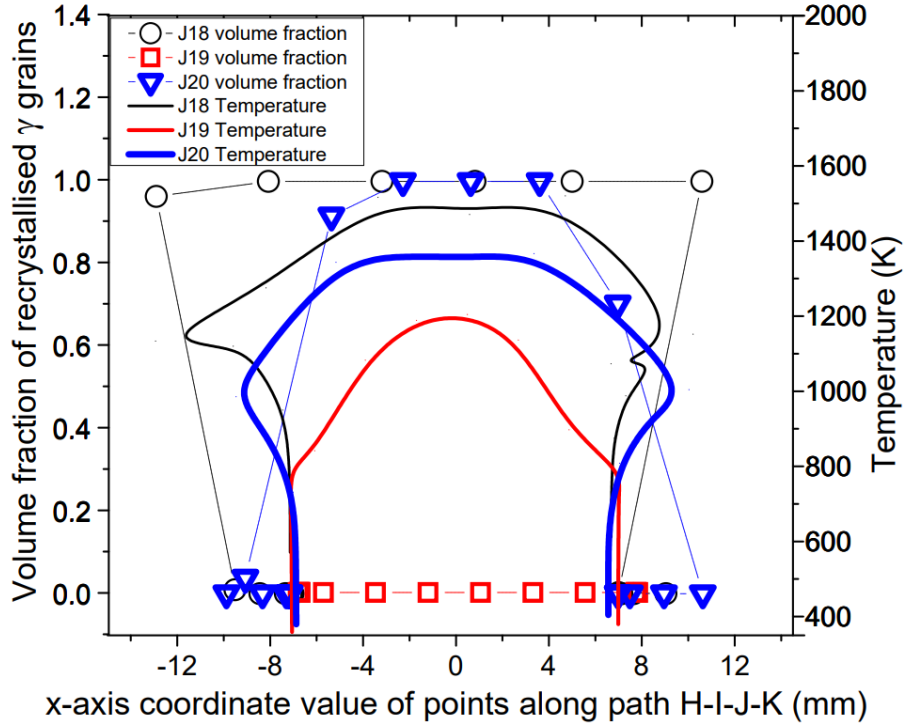


495

496

497

(f)



498

499

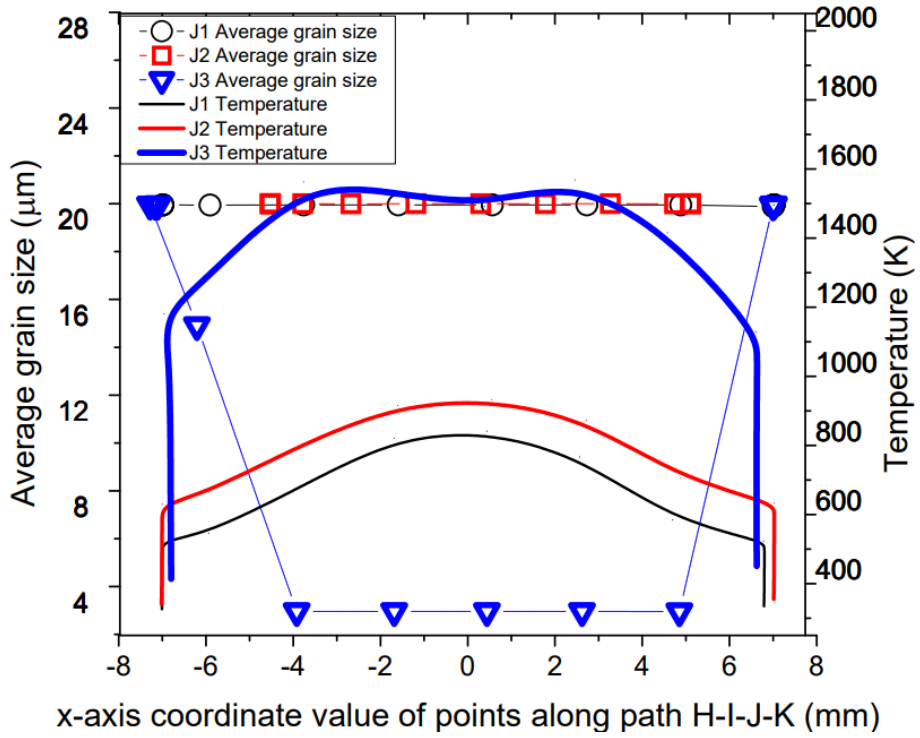
(g)

500 **Fig. 13** Computational modelling results of profile of volume fraction of recrystallised grains and
 501 temperature along the path H–I–J–K for LFW setups (a) J1, J2, and J3; (b) J4, J5, and J6; (c)
 502 J7, J8, and J9; (d) J10, J11, and J12; (e) J13, J14, and J15; (f) J16, J17, and J18; (g) J18, J19, and
 503 J20

504

505 For setups J1 and J2, there is low friction pressure $p_f = 100$ MPa, low oscillating frequency $f_0 \leq$
 506 20 Hz, small oscillating amplitude $A_0 = 2.5$ mm, and correspondingly low average rubbing
 507 velocity of $v_r \leq 200$ mm/s. Such setups could not result in significant plastic deformation, as
 508 discussed in the authors' previous work [33,34]. Although setup J3 is based on very low friction
 509 pressure $p_f = 100$ MPa, its frequency $f_0 = 40$ Hz and amplitude $A_0 = 3.3$ mm are at a very high
 510 level, resulting in significant weld deformation and DRX of γ grains. This is why significant grain
 511 refinement can be seen in Fig. 14(a) for setup J3.

512

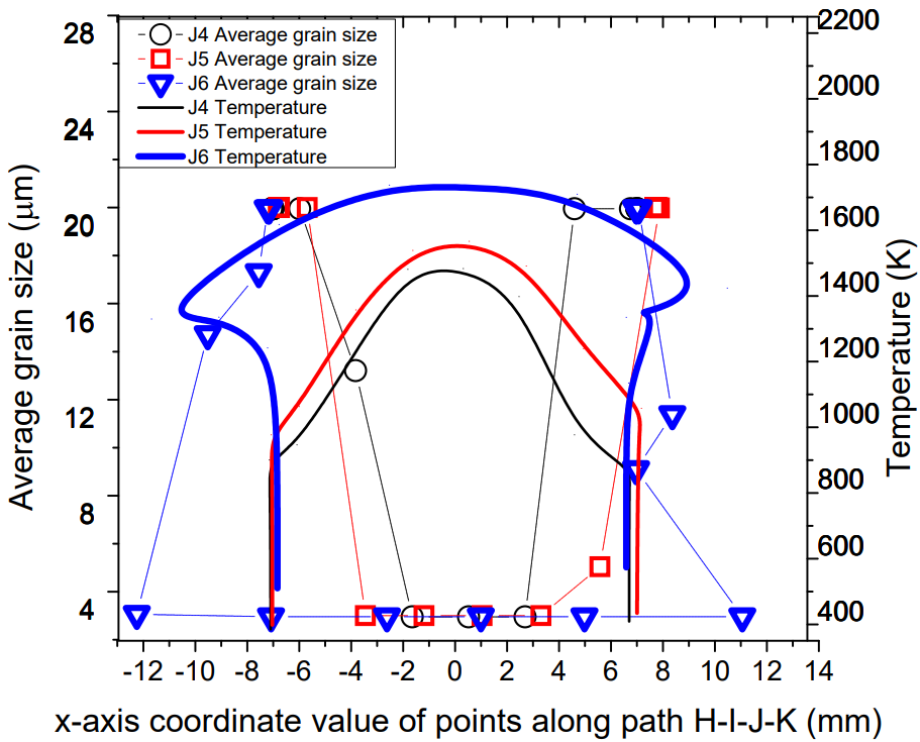


513

514

515

(a)

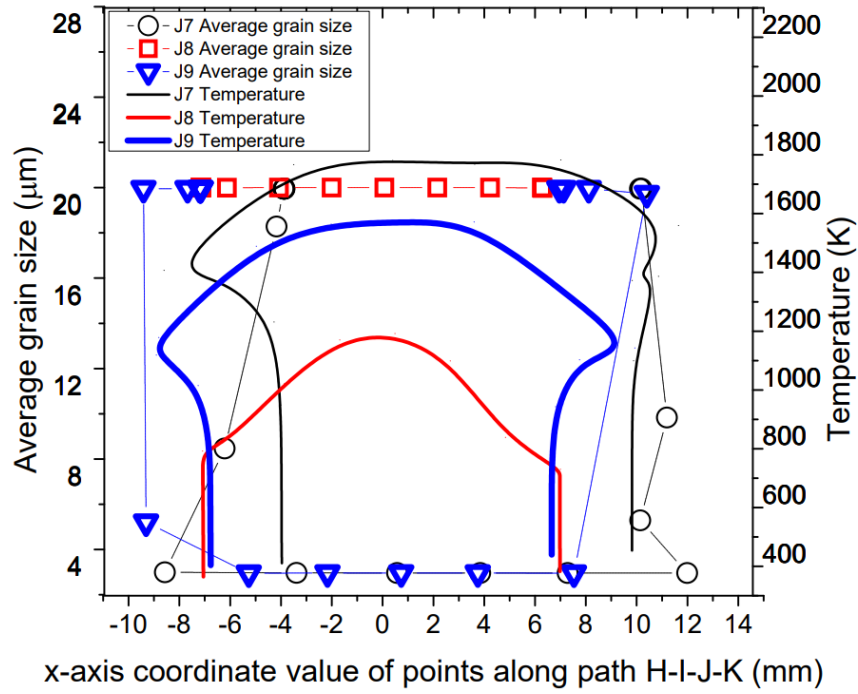


516

517

(b)

518

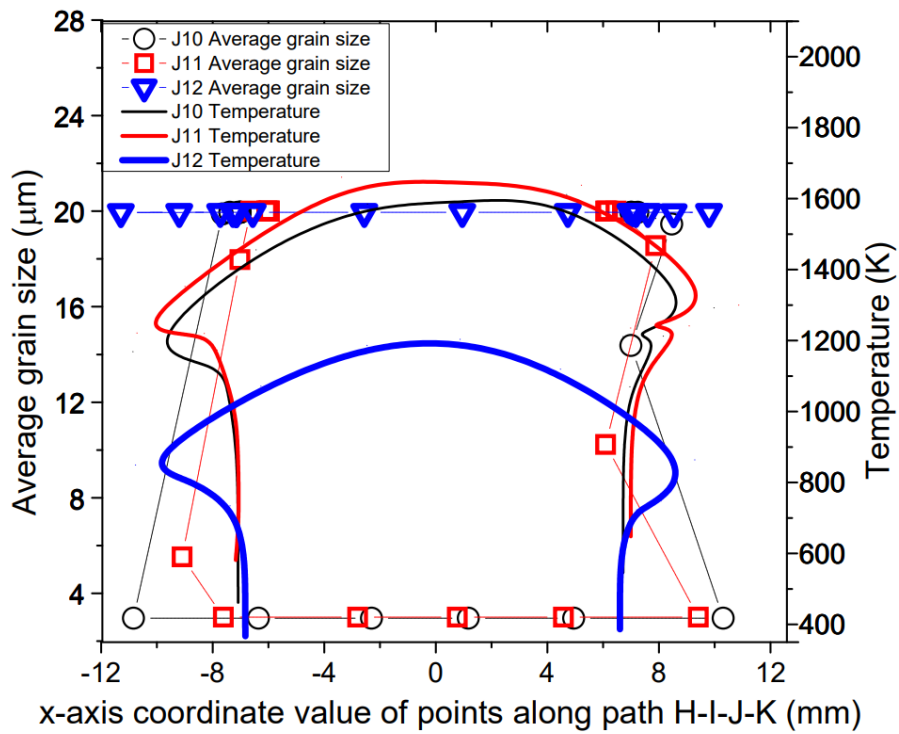


519

(c)

520

521

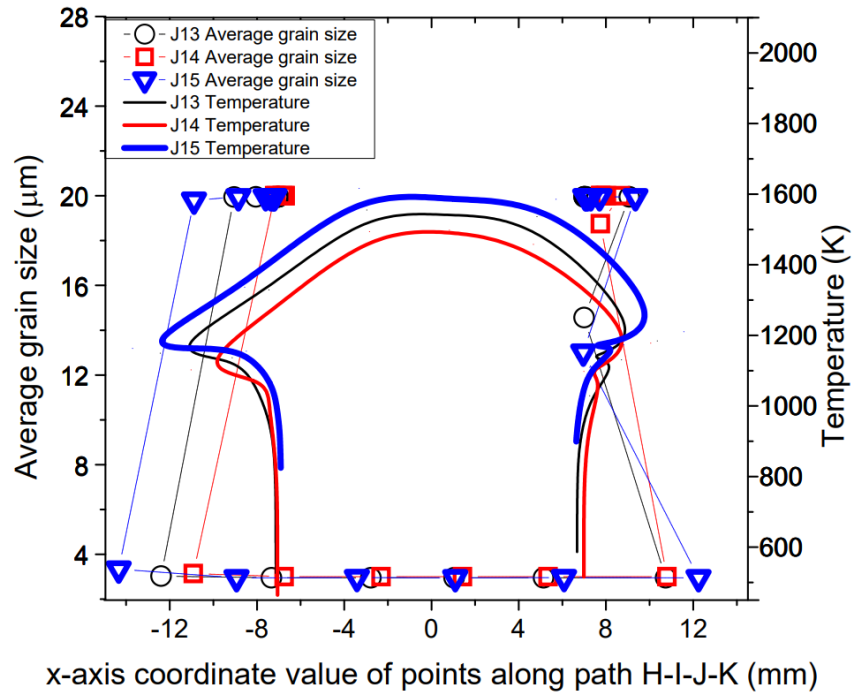


522

(d)

523

524

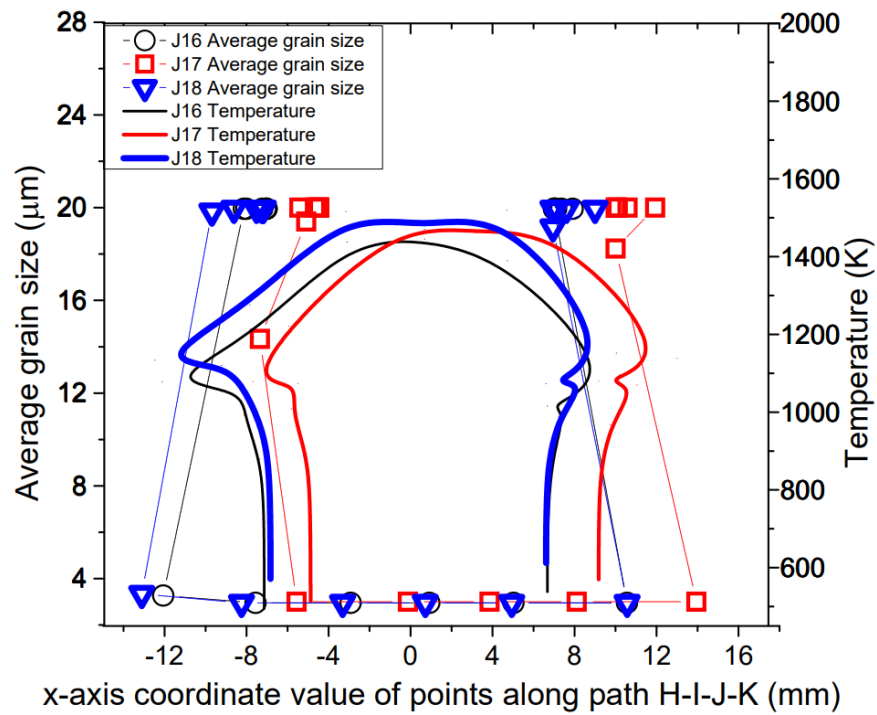


525

526

527

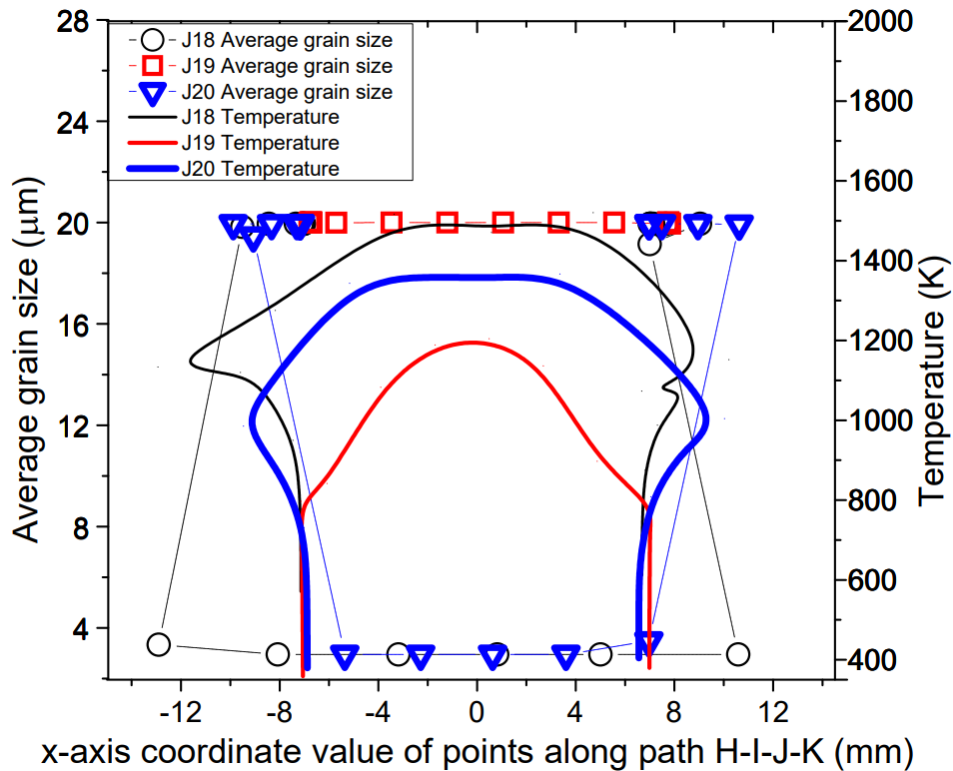
(e)



528

529

(f)



531

532

(g)

533 **Fig. 14** Computational modelling results of profile of average γ grain size and temperature along
 534 the path H–I–J–K for LFW setups (a) J1, J2, and J3; (b) J4, J5, and J6; (c) J7, J8, and J9; (d)
 535 J10, J11, and J12; (e) J13, J14, and J15; (f) J16, J17, and J18; (g) J18, J19 and J20

536

537 Figures 13(b–c) and 14(b–c) show that setups J4, J5, J6, J7, and J9 resulted in fully recrystallised
 538 and significantly refined γ grains within $x = \pm 1.9$ mm, ± 5.6 mm, ± 12.4 mm, ± 15.7 mm, and
 539 ± 8.7 mm, respectively, relative to the centre of friction interface. These setups have at least two
 540 LFW process parameters at a very high level, for instance, $p_f \geq 200$ MPa, $f_0 \geq 20$ Hz, $A_0 \geq$
 541 2.5 mm and $v_r \geq 264$ mm/s. The maximum friction interface temperatures of these setups in
 542 figures 13(b–c) and 14(b–c) are below the liquidus temperature of IN718 (no remelting
 543 occurred) except for setup J7 (1791 K), which is based on two extremely high levels of process
 544 parameters $f_0 = 40$ Hz and $A_0 = 3.3$ mm. Fully recrystallised and significantly refined grains can
 545 happen when running LFW using such extremely high levels of process parameters, which
 546 however can also cause extremely high weld temperature and excessive flash formation during
 547 LFW [20,35,40]. Although setup J3 is based on extremely high frequency and large amplitude like
 548 J7, it uses low friction pressure of 100 MPa, which does not cause a very high weld temperature
 549 that may exceed the liquidus temperature of IN718.

550 In figures 13(c – g) and 14(c – g), the results of setups J8, J12 and J19 are similar to those of J1
551 and J2, where no DRX and no grain refinement happened, and weld deformation was very little.
552 However, setups J10, J11, J13, J14, J15, J16, J17, J18, and J20 resulted in fully recrystallised and
553 significantly refined grains up to $x = \pm 11.0$ mm, ± 12.9 mm, ± 10.2 mm, ± 11.2 mm, ± 12.7 mm,
554 ± 11.8 mm, ± 11.7 mm, ± 13.1 mm, and ± 5.3 mm, respectively, relative to the centre of friction
555 interface. These setups have one process parameter at a low level, such as $p_f \leq 300$ MPa, $f_0 \leq$
556 20 Hz, $A_0 \leq 2.5$ mm, and $v_r \leq 264$ mm/s and the combination of at least two process parameters
557 at very high levels. The maximum friction interface temperatures of these setups in figures 13(c –
558 g) and 14(c – g) are below the liquidus temperature of IN718, thus no remelting occurred during
559 LFW. Path H–I–J–K was significantly elongated in the LFW setups that have $f_0 \geq 30$ Hz and
560 $A_0 \geq 2.9$ mm.

561 The overall results shown in figures 13(a – g) and 14(a – g) indicate that for different LFW setups,
562 DRX and grain refinement did not happen at the sides of the bottom workpiece (such as
563 approximately along paths H–I and J–K) due to relatively low temperature and plastic
564 deformation. However, depending on the specified process parameters, temperature levels higher
565 than the critical temperature for initiating DRX (~ 1213 K) were predicted near the centre of path
566 I–J (on the friction interface). Irrespective of the friction pressure, no DRX, grain refinement or
567 significant material deformation of the weld was obtained when $f_0 = 15$ Hz, $A_0 = 2.5$ mm, and
568 $v_r = 150$ mm/s (like setups J1, J8, J12, and J19). When friction pressure is low such as $p_f \leq$
569 200 MPa, either frequency $f_0 \geq 30$ Hz or amplitude $A_0 \geq 3.3$ mm needs to be at a very high level
570 in order to cause significant DRX and grain refinement on the friction interface. Besides setups J1,
571 J2, J8, J12, and J19, there is DRX happening either partially or completely in other LFW setups
572 along the path H–I–J–K (mostly on path I–J of weld). It can be seen in the modelling results that
573 partial or full DRX happens only when the temperature is higher than 1213 K.

574 When the LFW process parameters are all at high levels such that $p_f \geq 200$ MPa, $f_0 \geq 40$ Hz,
575 $A_0 \geq 3.3$ mm, and $v_r \geq 528$ mm/s, the maximum weld temperature can get higher than IN718
576 liquidus temperature, which indicates that remelting can occur at the friction interface. In terms of
577 computational modelling, such extreme LFW process parameters can cause difficulties in dynamic
578 remeshing of computational mesh during LFW process modelling [34,41]. In terms of the practical
579 LFW process, such extreme process parameters can result in excessive flash formation and axial
580 shortening.

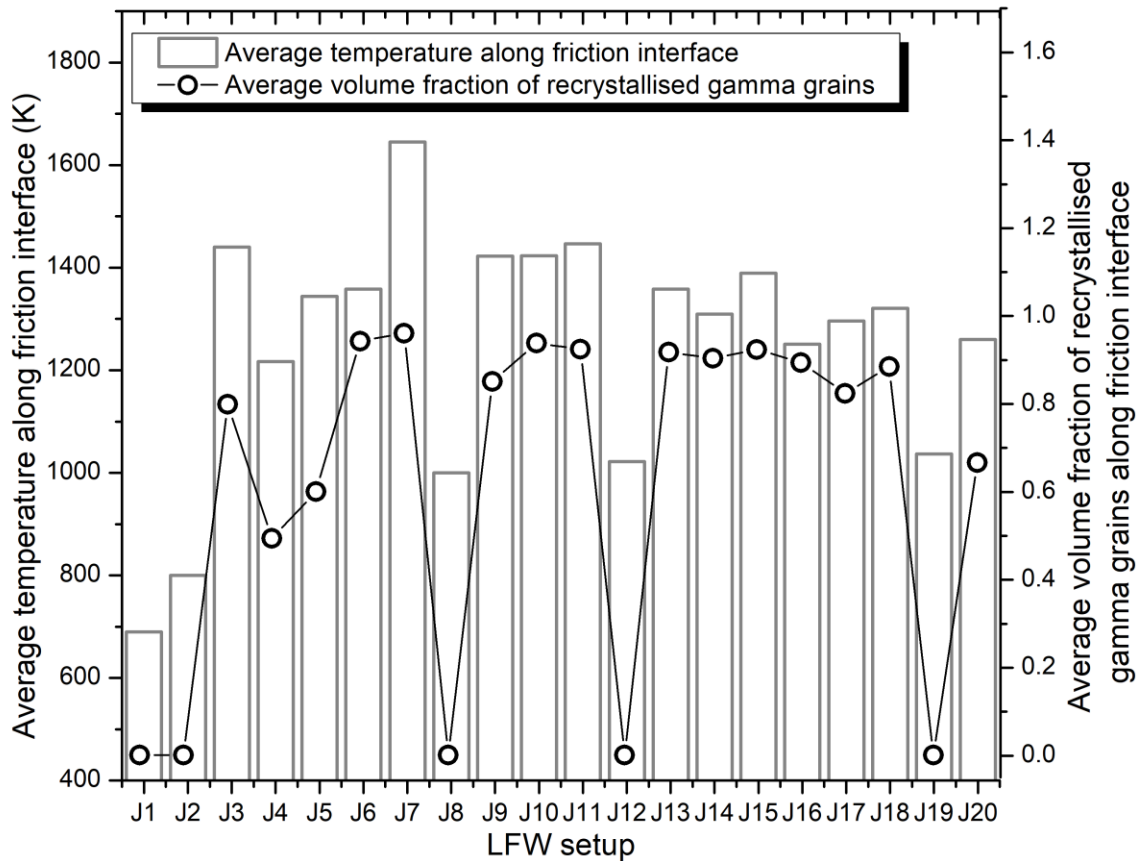
581 Figures 13(a – g) and 14(a – g) show that the weld material along path H–I–J–K was
582 significantly elongated for setups using $p_f \geq 200$ MPa, $f_0 \geq 30$ Hz, $A_0 \geq 2.9$ mm, and $v_r \geq$
583 348 mm/s (like setups J7, J11, and J15). For the same level of frequency and amplitude, the region
584 of material that gets fully recrystallised becomes larger when friction pressure increases from $p_f =$
585 100 MPa to $p_f = 600$ MPa (like the LFW setups J5, J10, J13, and J17). At the same level of
586 friction pressure, for instance, 300 MPa or 400 MPa (like in LFW setups J8, J9, J10, J11, J12, J13,
587 J14, and J15), the region of fully recrystallised material becomes larger when higher values of
588 frequency ($f_0 \geq 25$ Hz), amplitude ($A_0 \geq 2.9$ mm), and average rubbing velocity ($v_r \geq$
589 290 mm/s) are employed. The level of pressure turns out to be a critical parameter because there

590 is no DRX during LFW when $p_f \leq 200$ MPa regardless of the different levels of frequency and
591 amplitude that were tested in the computational modelling.

592

593 **3.3.2 LFW process window**

594 To determine the LFW process window, the modelling results of weld temperature, average γ grain
595 size, and axial shortening were considered for all 20 LFW setups. The modelling results of average
596 temperature and average volume fraction of recrystallised γ grains at the friction interface along
597 path I–J (bottom workpiece) at 5.0 s of welding for all 20 different LFW setups can be seen in
598 Fig. 15. The modelling results of average γ grain size at the friction interface and axial shortening
599 of top and bottom workpieces for all 20 different LFW setups at 5.0 s of welding can be seen in
600 Fig. 16. Overall, for all 20 different LFW setups, the average volume fraction of recrystallised γ
601 grains is high and the average γ grain size is small along path I–J when the average temperature
602 of friction interface is high. For all 20 LFW, average temperature, average volume fraction of
603 recrystallised γ grains, and average γ grain size at the friction interface are in the ranges of 691 –
604 1632 K, 0.01 – 95.0%, and 3.1 – 20.0 μm , respectively. No significant remelting occurred in any
605 LFW simulation.

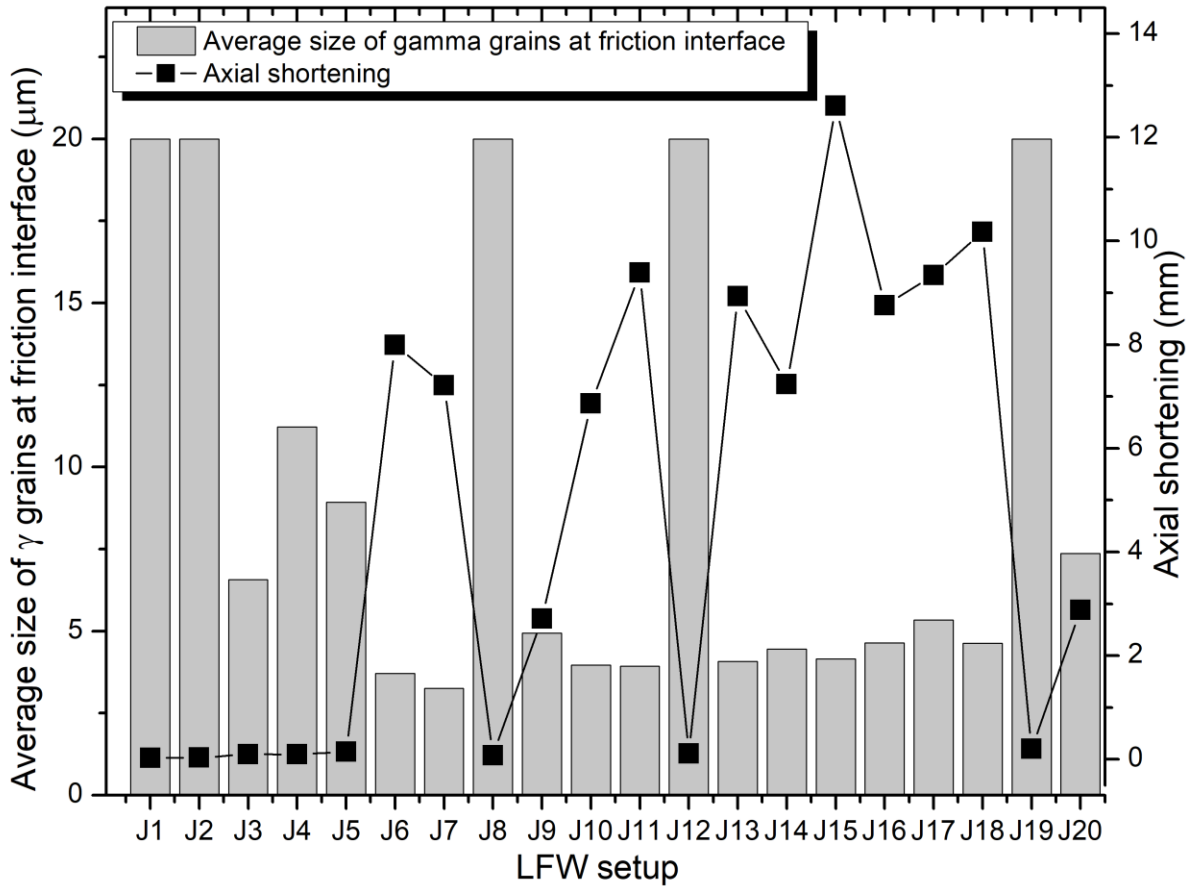


607

608 **Fig. 15** Computational modelling results of average temperature and average volume fraction of
 609 recrystallised γ grains along the friction interface at 5.0 s of welding for 20 different LFW setups

610

611 As shown in Fig. 16, axial shortening is low when $p_f = 100$ MPa irrespective of frequency and
 612 amplitude. Additionally, axial shortening is low when using $f_0 = 15$ Hz, $A_0 = 2.5$ mm (resulting
 613 in $v_r \geq 150$ mm/s), irrespective of pressure. Geng et al. recommended a critical (minimum)
 614 shortening length $L_a = 4.8$ mm, for achieving a reliable IN718 weld joint, that is satisfied by LFW
 615 setups J6, J7, J9 to J11, J13 to J18, and J20 [11]. All the setups that satisfied the critical shortening
 616 length also resulted in refined grains due to recrystallisation without material remelting at the
 617 friction interface.

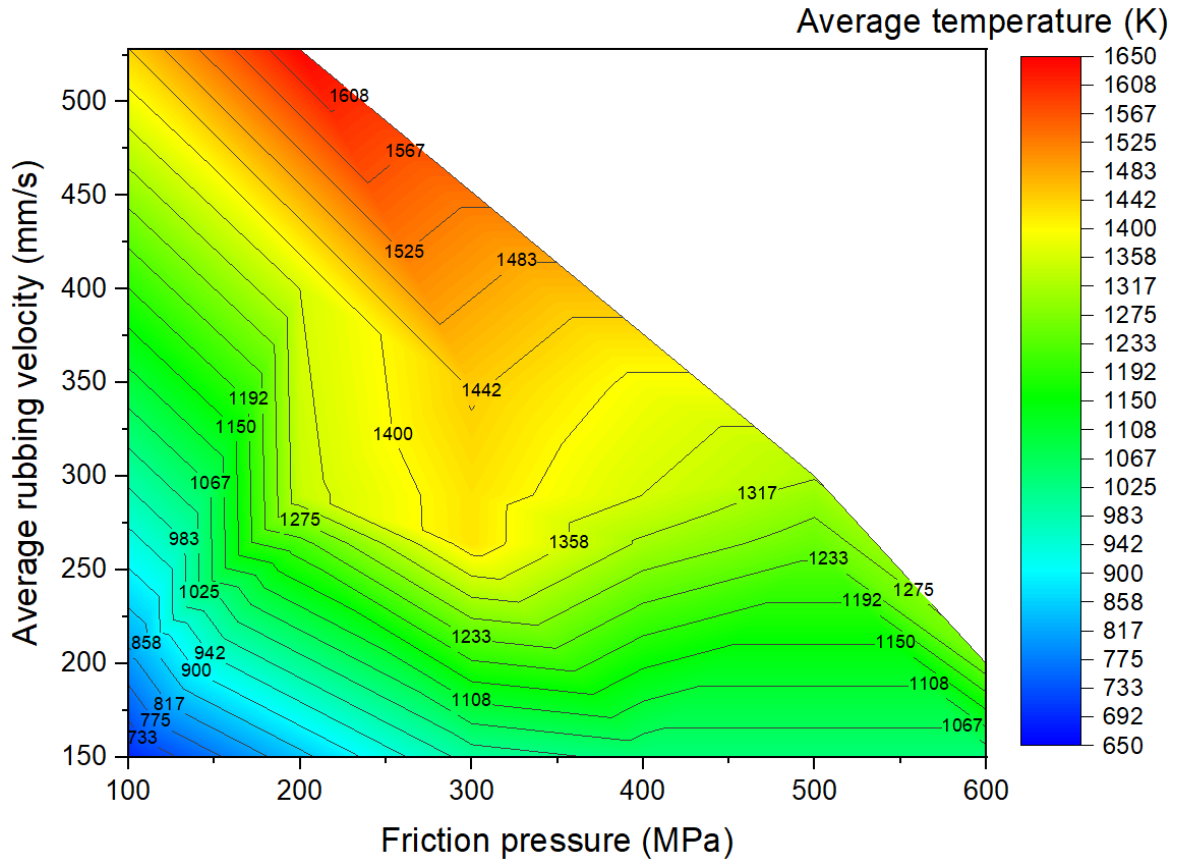


619

620 **Fig. 16** Computational modelling results of average γ grain size at friction interface and axial
 621 shortening of welds at 5.0 s of welding for 20 different LFW setups

622

623 Figures 17 to 19 show the LFW process windows that were created by using the computational
 624 modelling results (at 5.0 s of welding) of average rubbing velocity, friction pressure, average
 625 temperature along the friction interface, average γ grain size along the friction interface, and axial
 626 shortening for all 20 LFW setups. In the process windows, there are no computational modelling
 627 results for average rubbing velocity $v_r \geq 348$ mm/s and friction pressure $p_f \geq 400$ MPa, because
 628 such extreme process parameters caused excessive distortion of computational mesh and therefore
 629 corresponding computational simulation of related LFW process (at such extreme level of process
 630 parameters) could not be successfully completed.



631

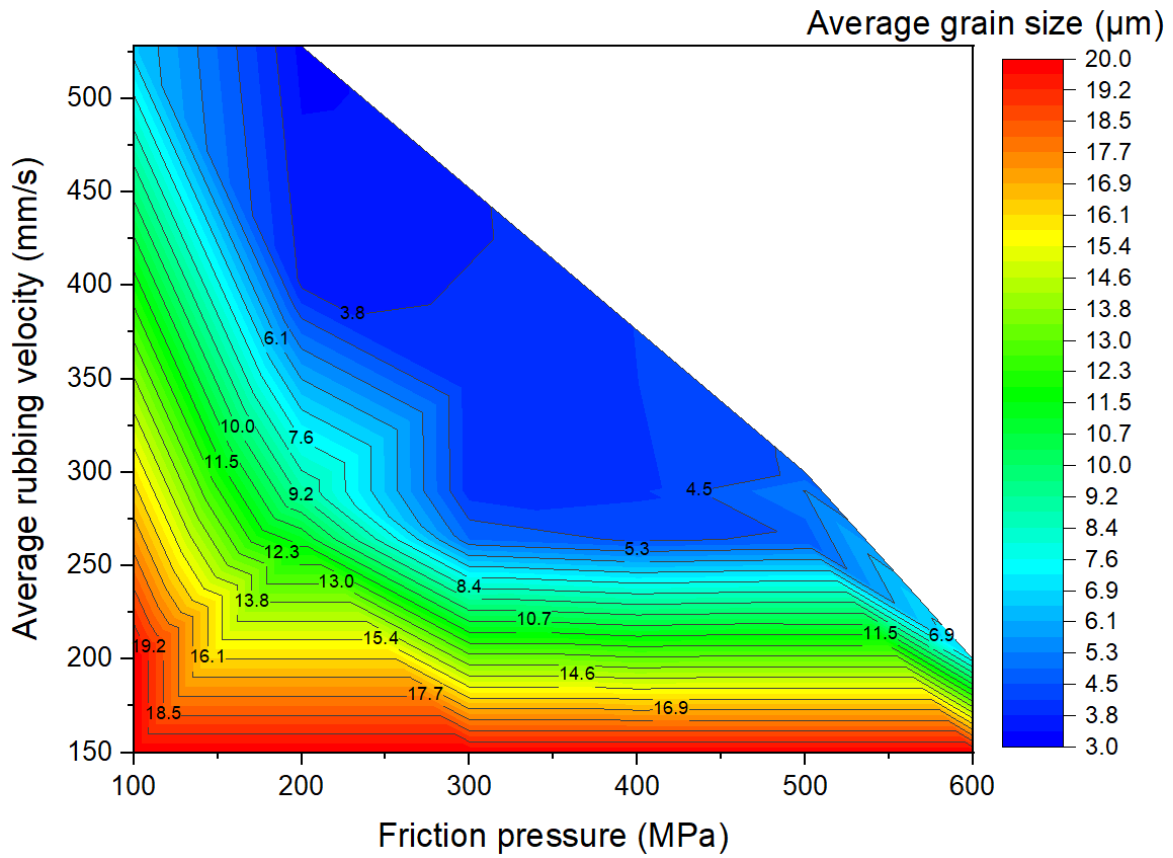
632

633

Fig. 17 Process window in terms of average temperature at friction interface, average rubbing velocity and friction pressure for 20 different LFW setups

634

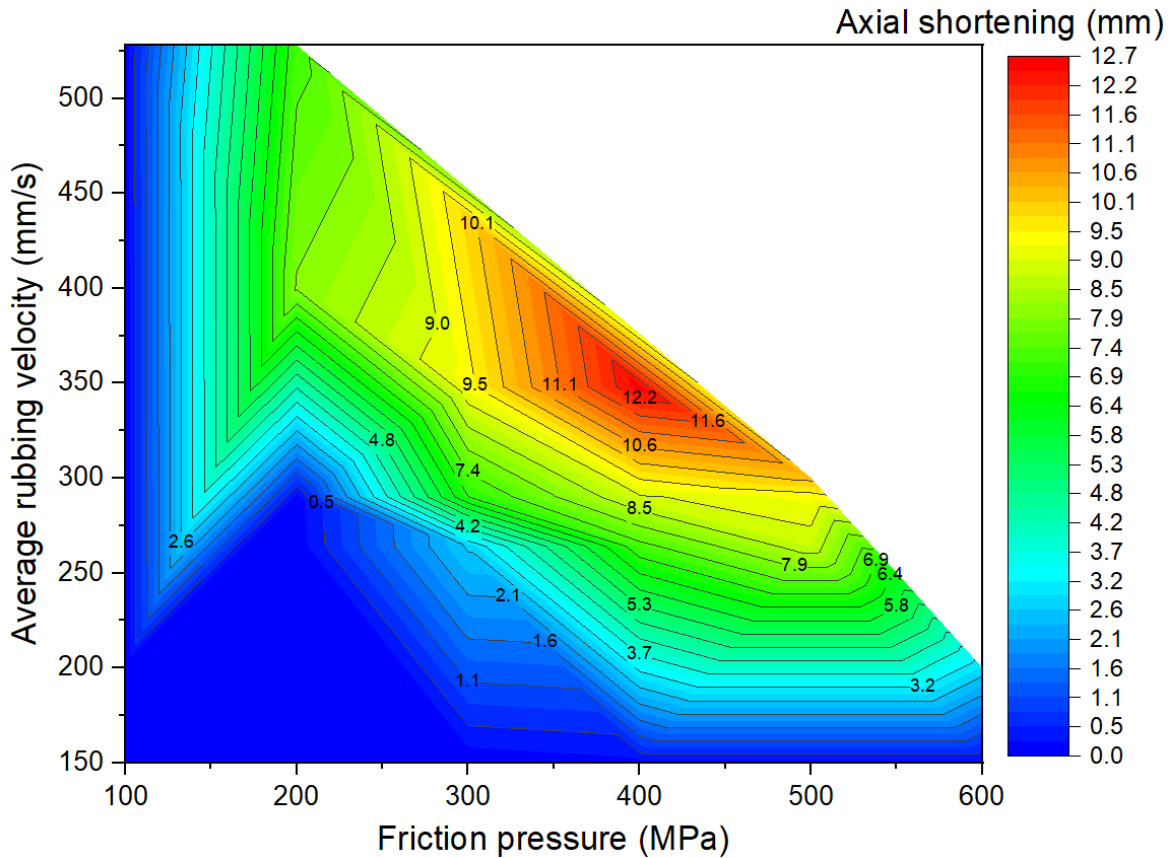
635



636

637 **Fig. 18** Process window in terms of average γ grain size at friction interface, average rubbing
638 velocity and friction pressure for 20 different LFW setups

639



641

642 **Fig. 19** Process window in terms of axial shortening, average rubbing velocity and friction
 643 pressure for 20 different LFW setups

644

645 In Fig. 17, it can be seen that high rubbing velocity results in high weld temperature, regardless of
 646 the different levels of friction pressure that were tested in the 20 different setups. This indicates
 647 that average rubbing velocity has a much more dominant influence on energy input for LFW than
 648 friction pressure. In figures 18 and 19, it can be seen that a high level of axial shortening and very
 649 significant grain refinement (due to DRX) can happen when there is a combination of high rubbing
 650 velocity and high friction pressure, for instance, when the friction pressure is approximately at the
 651 level of 400 MPa, and rubbing velocity approximately at the level of 350 mm/s. Geng et al.
 652 attributed sufficient axial shortening and fine γ grains to good weld bonding quality as well as good
 653 strength and hardness of the weld [11].

654 It can be concluded from the computational modelling results shown in figures 13 to 19 that high
 655 levels of friction pressure (≥ 200 MPa), oscillating frequency (≥ 25 Hz), oscillating amplitude (\geq
 656 2.9 mm), and average rubbing velocity (≥ 290 mm/s) result in high average temperature at the
 657 friction interface (≥ 1453 K), very small γ grain size (≤ 5.6 μm) due to DRX, and high axial
 658 shortening of the overall weld (≥ 5.8 mm). Friction pressure was found to be the most influential

659 process parameter and the least influential process parameter is oscillating amplitude, for
660 determining average temperature, average volume fraction of recrystallised γ grains, and average
661 γ grain size at the friction interface as well as axial shortening of welds.

662

663 **Conclusions**

664 In this study, integrated multiphysics computational modelling for LFW process was developed
665 by sequentially coupling a thermomechanical model with a microstructural model. Heat transfer,
666 elastic and plastic deformation of weld, and dynamic recrystallisation are in the modelling, which
667 predicts the results of LFW of IN718 in terms of such as weld temperature, plastic strain, volume
668 fraction of recrystallised γ grains, and resulting γ grain size as well as axial shortening of the overall
669 weld. For the first time, an integrated multiphysics computational modelling has been developed
670 for predicting LFW of IN718 at the scale of the overall weld. The integrated computational
671 modelling was verified by comparing its modelling results of γ grain size profile of weld with
672 related experimental results of other researchers [11].

673 The influence of process parameters (pressure, frequency, amplitude, and average rubbing
674 velocity) on predicting weld temperature, axial shortening, volume fraction of recrystallised γ
675 grains, and average γ grain size of IN718 LFW welds was systematically analyzed by using 20
676 different LFW setups in the computational modelling. Friction pressure (≥ 200 MPa) was found to
677 be the most significant process parameter influencing the recrystallisation of γ grains, as well as
678 weld temperature and axial shortening. High friction pressure results in high temperature and high
679 strain rate, which significantly drive dynamic recrystallisation of γ grains around the friction
680 interface of weld during LFW. Frequency and amplitude showed less significant influence
681 compared to friction pressure, and amplitude turns out to be the least influential LFW process
682 parameter. The related LFW process windows (figures 17 to 19) consistently show that at least
683 two LFW process parameters must be simultaneously at a very high level in order to achieve
684 sufficient axial shortening of overall weld (≥ 5.8 mm) and significantly refined γ grains (≤ 5.6 μm)
685 around the friction interface. The integrated computational modelling can effectively and
686 efficiently help the manufacturing industry to optimise the design of LFW process parameters.

687

688 **Acknowledgements**

689 The authors gratefully acknowledge the enabling computational modelling platform provided by
690 the Irish Centre for High-End Computing (ICHEC) Ireland.

691

692 **Authors Contributions**

693 Saviour I. Okeke: conceptualization, data curation, formal analysis, investigation, methodology,
694 software, verification, visualisation and writing—original draft.

695 Noel M. Harrison: funding acquisition, supervision and writing—review and editing.

696 Mingming Tong: funding acquisition, supervision, conceptualization, project management and
697 writing—review and editing.

698

699 **Funding Information**

700 This study was supported by School of Engineering, College of Science and Engineering
701 Postgraduate Scholarship, National University of Ireland Galway. This publication has emanated
702 from research supported in part by a grant from Science Foundation Ireland under Grant number
703 16/RC/3872. For the purpose of Open Access, the author has applied a CC BY public copyright
704 licence to any Author Accepted Manuscript version arising from this submission.

705

706 **Availability of data and material**

707 The data used to support the findings of this study are available from the funding source on
708 demand.

709

Declarations

Ethical Approval

Not applicable

Consent to Participate

Not applicable

Consent to Publish

Not applicable

Competing Interest

The authors declare no competing interests.

References

1. McAndrew AR, Colegrove PA, Buhr C, Flipo BCD, Vairis A (2018) A literature review of Ti-6Al-4V linear friction welding. *Progress in Materials Science* 92:225-257. <https://doi.org/10.1016/j.pmatsci.2017.10.003>
2. Turner R, Gebelin JC, Ward RM, Reed RC (2011) Linear friction welding of Ti-6Al-4V: Modelling and validation. *Acta Materialia* 59 (10):3792-3803. <https://doi.org/10.1016/j.actamat.2011.02.028>
3. Bhamji I, Preuss M, Threadgill PL, Addison AC (2011) Solid state joining of metals by linear friction welding: a literature review. *Material Science and Technology* 27:2-12. <https://doi.org/10.1179/026708310X520510>
4. Geng P, Qin G, Zhou J, Li C (2019) Parametric optimization and microstructural characterization of friction welded aeronautic aluminum alloy 2024. *Transactions of Nonferrous Metals Society of China* 29 (12):2483-2495. [https://doi.org/10.1016/s1003-6326\(19\)65156-3](https://doi.org/10.1016/s1003-6326(19)65156-3)
5. Bhamji I, Preuss M, Threadgill PL, Moat RJ, Addison AC, Peel MJ (2010) Linear friction welding of AISI 316L stainless steel. *Mat Sci Eng a-Struct* 528 (2):680-690. <https://doi.org/10.1016/j.msea.2010.09.043>
6. Grujicic M, Yavari R, Snipes JS, Ramaswami S, Yen CF, Cheeseman BA (2014) Linear friction welding process model for Carpenter Custom 465 precipitation-hardened martensitic stainless steel. *J Mater Eng Perform* 23 (6):2182-2198. <https://doi.org/10.1007/s11665-014-0985-9>
7. Grujicic M, Yavari R, Snipes JS, Ramaswami S (2014) A linear friction welding process model for Carpenter Custom 465 precipitation-hardened martensitic stainless steel: A weld microstructure-evolution analysis. *Proceedings of the Institution of Mechanical Engineers, Part B: Journal of Engineering Manufacture* 229 (11):1997-2020. <https://doi.org/10.1177/0954405414542137>

8. Chamanfar A, Jahazi M, Cormier J (2015) A review on inertia and linear friction welding of Ni-based superalloys. *Metall Mater Trans A* 46a (4):1639-1669. <https://doi.org/10.1007/s11661-015-2752-4>
9. Mateo-Garcia AM (2011) BLISK fabrication by linear friction welding. *Advances in Gas Turbine Technology*:411-434. <https://doi.org/10.5772/21278>
10. Reed RC (2006) *The superalloys: fundamentals and applications*. Cambridge University Press, Cambridge, England
11. Geng P, Qin G, Li T, Zhou J, Zou Z, Yang F (2019) Microstructural characterization and mechanical property of GH4169 superalloy joints obtained by linear friction welding. *Journal of Manufacturing Processes* 45:100-114. <https://doi.org/10.1016/j.jmapro.2019.06.032>
12. Azadian S, Wei LY, Warren R (2004) Delta phase precipitation in Inconel 718. *Mater Charact* 53 (1):7-16. <https://doi.org/10.1016/j.matchar.2004.07.004>
13. Beaubois V, Huez J, Coste S, Brucelle O, Lacaze J (2004) Short term precipitation kinetics of delta phase in strain free Inconel 718 alloy. *Material Science and Technology* 20 (8):1019-1026. <https://doi.org/10.1179/026708304225019830>
14. Radavich JF (1989) The physical metallurgy of cast and wrought alloy 718. *Superalloy 718—Metallurgy and Applications*:229-240. https://doi.org/10.7449/1989/Superalloys_1989_229_240
15. Vishwakarma KR, Ojo OA, Wanjara P, Chaturvedi MC (2014) Microstructural analysis of linear friction-welded 718 plus superalloy. *JOM* 66 (12):2525-2534. <https://doi.org/10.1007/s11837-014-0938-7>
16. Mary C, Jahazi M (2008) Multi-scale analysis of IN-718 microstructure evolution during linear friction welding. *Adv Eng Mater* 10:573-578. <https://doi.org/10.1002/adem.200700361>
17. Mary C, Jahazi M (2007) Linear friction welding of IN-718 process optimization and microstructure evolution. *5th International Conference on Processing and Manufacturing of Advanced Materials, Coll Advanced Materials Research: Trans Tech Publications* 15-17: 357-362. <https://doi.org/10.4028/www.scientific.net/AMR.15-17.357>
18. Ma TJ, Chen X, Li WY, Yang XW, Zhang Y, Yang SQ (2016) Microstructure and mechanical property of linear friction welded nickel-based superalloy joint. *Mater Design* 89:85-93. <https://doi.org/10.1016/j.matdes.2015.09.143>
19. Markov O, Gerasimenko O, Aliieva L, Shapoval A (2019) Development of the Metal Rheology Model of High-Temperature Deformation for Modeling by Finite Element Method. *EUREKA: Physics and Engineering* 2:52-60. <https://doi.org/10.21303/2461-4262.2019.00877>
20. Qin GL, Geng PH, Zhou J, Zou ZD (2019) Modeling of thermo-mechanical coupling in linear friction welding of Ni-based superalloy. *Mater Design* 172:1-18. <https://doi.org/10.1016/j.matdes.2019.107766>
21. Yang J (2014) *Microstructure-property development in linear friction welding of nickel-based superalloys*. PhD thesis, The University of Birmingham
22. Smith M, Bichler L, Gholipour J, Wanjara P (2016) Mechanical properties and microstructural evolution of in-service Inconel 718 superalloy repaired by linear friction welding. *The International Journal of Advanced Manufacturing Technology* 90 (5-8):1931-1946. <https://doi.org/10.1007/s00170-016-9515-2>
23. Chamanfar A, Jahazi M, Gholipour J, Wanjara P, Yue S (2012) Suppressed liquation and microcracking in linear friction welded WASPALOY. *Material and Design* 36:113–122. <https://doi.org/10.1016/j.matdes.2011.11.007>

24. Chamanfar A, Jahazi M, Gholipour J, Wanjara P, Yue S (2012) Maximizing the integrity of linear friction welded Waspaloy. *Materials Science and Engineering: A* 555:117-130. <https://doi.org/10.1016/j.msea.2012.06.041>
25. Chamanfar A, Jahazi M, Gholipour J, Wanjara P, Yue S (2011) Mechanical property and microstructure of linear friction welded Waspaloy. *Metall Mater Trans A* 42a (3):729-744. <https://doi.org/10.1007/s11661-010-0457-2>
26. Preuss M, Withers PJ, Pang JWL, Baxter GJ (2002) Inertia welding nickel-based superalloy: Part I. Metallurgical characterization. *Metallurgical and Materials Transactions A* 33:3215–3225. <https://doi.org/10.1007/s11661-002-0307-y>
27. Huang Z. W. LHY, Baxter G., Bray S., Bowen P. (2011) Electron microscopy characterization of the weld line zones of an inertia friction welded superalloy. *J Mater Process Technol* 211:1927-1936. <https://doi.org/10.1016/j.jmatprotec.2011.06.019>
28. Huang ZW, Li HY, Baxter G, Bray S, Bowen P (2011) Characterization of the Weld Line Zones of an Inertia Friction Welded Superalloy. *Advanced Materials Research* 278:440-445. <https://doi.org/10.4028/www.scientific.net/AMR.278.440>
29. Li WY, Vairis A, Preuss M, Ma TJ (2016) Linear and rotary friction welding review. *Int Mater Rev* 61 (2):71-100. <https://doi.org/10.1080/09506608.2015.1109214>
30. Geng P, Qin G, Zhou J, Li T, Ma N (2021) Characterization of microstructures and hot-compressive behavior of GH4169 superalloy by kinetics analysis and simulation. *Journal of Materials Processing Technology* 288:116879. <https://doi.org/10.1016/j.jmatprotec.2020.116879>
31. Chamanfar A, Jahazi M, Gholipour J, Wanjara P, Yue S (2013) Modeling Grain Size and Strain Rate in Linear Friction Welded Waspaloy. *Metallurgical and Materials Transactions A* 44 (9):4230-4238. <https://doi.org/10.1007/s11661-013-1767-y>
32. Tabaie S, Rézai-Aria F, Flipo BCD, Jahazi M (2022) Dissimilar linear friction welding of selective laser melted Inconel 718 to forged Ni-based superalloy AD730™: Evolution of strengthening phases. *Journal of Materials Science & Technology* 96:248-261. <https://doi.org/10.1016/j.jmst.2021.03.086>
33. Okeke SI, Harrison N, Tong M (2020) Thermomechanical modelling for the linear friction welding process of Ni-based superalloy and verification. *Proc IMechE Part L: J Materials: Design and Applications* 234 (5):1-20. <https://doi.org/10.1177/1464420719900780>
34. Okeke SI, Harrison NM, Tong M (2021) Dissolution of delta phase in Ni-based superalloy during linear friction welding: integrated multiphysics computational process modelling. *The International Journal of Advanced Manufacturing Technology*. <https://doi.org/10.1007/s00170-021-07404-9>
35. Geng PH, Qin GL, Chen L, Zhou J, Zou ZD (2019) Simulation of plastic flow driven by periodically alternating pressure and related deformation mechanism in linear friction welding. *Mater Design* 178. <https://doi.org/10.1016/j.matdes.2019.107863>
36. Masoumi F, Shahriari D, Monajati H, Cormier J, Flipo BCD, Devaux A, Jahazi M (2019) Linear friction welding of AD730™ Ni-base superalloy: Process-microstructure-property interactions. *Mater Design* 183. <https://doi.org/10.1016/j.matdes.2019.108117>
37. Wang FF, Li WY, Li JL, Vairis A (2014) Process parameter analysis of inertia friction welding nickel-based superalloy. *International Journal of Advanced Manufacturing Technology* 71 (9-12):1909-1918. <https://doi.org/10.1007/s00170-013-5569-6>
38. Wang X, Li W, Ma T, Yang X, Vairis A (2019) Effect of welding parameters on the microstructure and mechanical properties of linear friction welded Ti-6.5Al-3.5Mo-1.5Zr-0.3Si

38. joints. *Journal of Manufacturing Processes* 46:100-108. <https://doi.org/10.1016/j.jmapro.2019.08.031>
39. Xie Y, Meng X, Li Y, Mao D, Wan L, Huang Y (2021) Insight into ultra-refined grains of aluminum matrix composites via deformation-driven metallurgy. *Composites Communications* 26. <https://doi.org/10.1016/j.coco.2021.100776>
40. Geng P, Qin G, Zhou J (2020) A computational modeling of fully friction contact-interaction in linear friction welding of Ni-based superalloys. *Mater Design* 185. <https://doi.org/10.1016/j.matdes.2019.108244>
41. Geng PH, Qin GL, Zhou J, Zou ZD (2019) Finite element models of friction behaviour in linear friction welding of a Ni-based superalloy. *International Journal of Mechanical Sciences* 152:420-431. <https://doi.org/10.1016/j.ijmecsci.2019.01.014>
42. Yang XW, Li WY, Li JL, Xiao B, Ma TJ, Huang Z, Guo J (2015) Finite element modeling of the linear friction welding of GH4169 superalloy. *Mater Design* 87:215-230. <https://doi.org/10.1016/j.matdes.2015.08.036>
43. Geng P, Qin G, Li T, Zhou J, Zou Z (2018) Hot deformation behavior and constitutive model of GH4169 superalloy for linear friction welding process. *Journal of Manufacturing Processes* 32:469-481. <https://doi.org/10.1016/j.jmapro.2018.03.017>
44. Geng P, Qin G, Li C, Wang H, Zhou J (2020) Study on the importance of thermo-elastic effects in FE simulations of linear friction welding. *Journal of Manufacturing Processes* 56:602-615. <https://doi.org/10.1016/j.jmapro.2020.05.051>
45. Geng P, Qin G, Ma H, Zhou J, Ma N (2021) Linear friction welding of dissimilar Ni-based superalloys: microstructure evolution and thermo-mechanical interaction. *J Mater Res Technol* 11:633-649. <https://doi.org/10.1016/j.jmrt.2021.01.036>
46. Tekkaya B, Meurer M, Münstermann S (2020) Modelling of Grain Size Evolution with Different Approaches via FEM When Hard Machining of AISI 4140. *Metals* 10 (10):1296. <https://doi.org/10.3390/met10101296>
47. Gao Z, Feng J, Wang Z, Niu J, Sommitsch C (2019) Dislocation Density-Based Modeling of Dynamic Recrystallized Microstructure and Process in Friction Stir Spot Welding of AA6082. *Metals* 9 (6):672. <https://doi.org/10.3390/met9060672>
48. Yang C, Wu C, Gao S (2021) Modified constitutive equation by using phase field simulation of dynamic recrystallization in friction stir welding. *J Mater Res Technol* 12:916-929. <https://doi.org/10.1016/j.jmrt.2021.03.031>
49. Tamirisakandala S, Vedam BV, Bhat RB (2003) Recent Advances in the Deformation Processing of Titanium Alloys. *J Mater Eng Perform* 12 (6):661-673. <https://doi.org/10.1361/105994903322692466>
50. Honarmandi P, Aghaie-Khafri M (2012) Hot Deformation Behavior of Ti-6Al-4V Alloy in β Phase Field and Low Strain Rate. *Metallography, Microstructure, and Analysis* 2 (1):13-20. <https://doi.org/10.1007/s13632-012-0052-6>
51. Na Y-S, Yeom J-T, Park N-K, Lee J-Y (2003) Simulation of microstructures for Alloy 718 blade forging using 3D FEM simulator. *Journal of Materials Processing Technology* 141 (3):337-342. [https://doi.org/10.1016/s0924-0136\(03\)00285-1](https://doi.org/10.1016/s0924-0136(03)00285-1)
52. Lin J, Dean, T. A. (2005) Modelling of microstructure evolution in hot forming using unified constitutive equations. *J Mater Process Technol* 167:354-362. <https://doi.org/10.1016/j.jmatprotec.2005.06.026>
53. Fanfoni M, Tomellini M (1998) The Johnson-Mehl- Avrami-Kohnogorov model: A brief review. *Il Nuovo Cimento D* 20 (7-8):1171-1182. <https://doi.org/10.1007/BF03185527>

54. Akram J, Kalvala PR, Jindal V, Misra M (2017) Evaluating location specific strain rates, temperatures, and accumulated strains in friction welds through microstructure modeling. *Defence Technology*. <https://doi.org/10.1016/j.dt.2017.11.002>.
55. Dassault-Systèmes (2017) Abaqus 2017 Analysis User's Guide Volume II: Analysis. <https://www.3ds.com/products-services/simulia/services-support/support/documentation/>
Accessed 14th May 2020
56. Schmidt H, Hattel J (2005) A local model for the thermomechanical conditions in friction stir welding. *Modelling and Simulation in Materials Science and Engineering* 13 (1):77-93. <https://doi.org/10.1088/0965-0393/13/1/006>
57. Maalekian M, Kozeschnik E, Brantner HP, Cerjak H (2008) Comparative analysis of heat generation in friction welding of steel bars. *Acta Materialia* 56:2843–2855. <https://doi.org/10.1016/j.actamat.2008.02.016>
58. Yanagimoto J, Karhausen K, Brand AJ, Kopp R (1998) Incremental Formulation for the Prediction of Flow Stress and Microstructural Change in Hot Forming. *Journal of Manufacturing Science and Engineering* 120 (2):316-322. <https://doi.org/10.1115/1.2830129>
59. Chen X-M, Lin YC, Wen D-X, Zhang J-L, He M (2014) Dynamic recrystallization behavior of a typical nickel-based superalloy during hot deformation. *Mater Design* 57:568-577. <http://dx.doi.org/10.1016/j.matdes.2013.12.072>